Past fires and post-fire impacts reconstructed from a southwest Australian stalagmite

Liza K. McDonough [a,*], Pauline C. Treble [a,b], Andy Baker [b,a], Andrea Borsato [c],
Silvia Frisia [c,b], Gurinder Nagra [d,b], Katie Coleborn [b], Michael K. Gagan [e,f],
Jian-xin Zhao [g], David Paterson [h]

[a] ANSTO, Lucas Heights, NSW 2234, Australia
[b] School of Biological, Earth and Environmental Sciences, University of New South Wales, Sydney, NSW 2052, Australia
[c] School of Environmental and Life Sciences, University of Newcastle, NSW 2308, Australia
[d] School of Earth, Energy and Environmental Sciences, Stanford University, CA 94305, USA
[e] School of Earth, Atmospheric and Life Sciences, University of Wollongong, NSW 2522, Australia
[f] School of Earth and Environmental Sciences, The University of Queensland, Brisbane, QLD 4072, Australia
[g] Radiogenic Isotope Facility, School of Earth and Environmental Sciences, The University of Queensland, Brisbane, QLD 4072, Australia
[h] Australian Synchrotron ANSTO, Clayton, VIC 3168, Australia

Abstract

Speleothem records of past environmental change provide an important opportunity to explore fire frequency and intensity in the past, and the antecedent climatic conditions leading to fire events. Here, fire sensitive geochemical signals in a stalagmite from Yonderup Cave, a shallow cave in Western Australia, are compared to well-documented wildfire events that occurred in recent decades. The results are extended to identify wildfires during the growth interval of the speleothem (1760 CE–2005 CE). Principal component analysis of the stalagmite time-series revealed distinct peaks in a combination of phosphorus and metal (aluminium, zinc, copper and lead) concentrations in response to known fire events, which are interpreted to have come from ash. Varying responses in the geochemical signal in the pre- and post-European colonisation period are likely linked to changes in land management, fire frequency and fire intensities. Of note is what we infer to be a particularly intense fire event concluded to have occurred in 1897 $\pm$ 5 CE, which climate sensitive proxies (δ^{18}O and bedrock-derived elements) indicate was preceded by a multi-decadal dry period that began in the late 1860s. The intensity of the deduced fire event is supported by a peak in P that is 6.3 times higher than elsewhere in the speleothem, accompanied by a peak in Zn. It was also inferred that changes to the surface-cave hydrology occurred as a result of this event, indicated by increased input of colloidal organic material onto the stalagmite that was interpreted to be caused by shallow karst bedrock fracturing from the heat-induced deformation that is observed after intense fires. These findings show the potential for speleothems to provide dated records of fire intensity and recurrence intervals. Further development could lead to a better understanding of the climate-fire relationship and the effects of land-management practices on wildfire frequency and intensity.

* Corresponding author.
  E-mail address: lizam@ansto.gov.au (L.K. McDonough).

1. INTRODUCTION

Wildfires are becoming progressively more extreme due to climate and land use changes (Moreira et al., 2020). Catastrophic wildfires such as those observed in Australia between October 2019 and February 2020, during which nearly 170,000 km^2 of land were burned are occurring with increasing frequency. In the Northern hemisphere, in 2020 more than 17,000 km^2 of land in the state of California were burned. Karst systems, where caves host speleothems (e.g., stalagmites, stalactites and flowstones), can provide long-term records of changes in climate and the environment (e.g. Bar-Matthews et al., 1997; Cheng et al., 2016; Dorale et al.,1998; Hellstrom et al., 1998; Hopley et al., 2007; Wang et al., 2008). The impact of wildfires on dripwater and soil in karst systems is becoming increasingly well understood (Coleborn et al., 2016; Nagra et al., 2016; Treble et al., 2016; Bian et al., 2019), and suggests that speleothems may have the potential to provide records of fire frequency and intensity. In this study, we investigate the geochemical 'fingerprint' of known fire events in a stalagmite from Western Australia, and extend this information to construct the first speleothem-based record of paleo-fire events. Utilising stalagmites as proxies for paleo-fire could provide much-needed baseline information for the pre-satellite period, including the timing of human arrival in a region, and the relationships between humans, environment, climate and fire.

Fires have the potential to alter soil properties and soluble element concentrations, which in turn affects soil leachate and dripwater chemistry. Variability in soil and ash leachate chemistry are impacted by the type of vegetation burnt and the burn intensity (Plumlee et al., 2007; Hogue and Inglett, 2012; Heydari et al., 2017; Harper et al., 2019; Quigley et al., 2019). Low to moderate intensity fires, such as prescribed burns, have been shown to result in increasing soil nutrients, whilst high intensity wildfires can potentially result in a reduction in nutrients due to volatilisation (Certini, 2005; Bodí et al., 2014). More generally, post-fire increases in soil nitrogen (N) and phosphorus (P) and sulphur (S) have been noted in a number of studies (Grove et al., 1986; Spencer et al., 2003; Schaller et al., 2015; Butler et al., 2018), as well as increases in organic matter (OM) and sediment flushed into waterways after fires (Petticrew et al., 2006; Mast and Clow, 2008; Ryan et al., 2011; Revchuk and Suffet, 2014). Furthermore, the formation of a hydrophobic soil layer has been observed following low intensity fire events, which may either increase surface run-off or preferential flow through the bedrock as excess water would not be retained in the soil (Savage, 1974; DeBano, 2000; Stoof et al., 2014; Bian et al., 2019). In contrast, water repellency can be eliminated at high temperatures (> 400 °C) due to the thermal destruction of hydrophobic OM (Dlapa et al., 2008), thereby increasing overall soil hydraulic conductivity (Quigley et al., 2021). These changes at the surface translate into changes in dripwater chemistry and can ultimately impact on speleothem composition. For example, short-term increases in dripwater elements such as S have previously been observed post-fire due to release of S from burnt vegetation (Bian et al., 2019) and evaporative concentration (Nagra et al., 2016). Decreases in S post-fire have also been observed due to nutrient limitation during forest regrowth (Treble et al., 2016), as well as temporary increase in dripwater δ^{18}O resulting from the evaporative loss of stored karst water (Nagra et al., 2016).

Temperatures above 500 °C can affect the structural properties of limestone (Wu and Wang, 2012; Meng et al., 2020), leading to the creation and/or widening of microfractures in the epikarst (the upper weathered region of bedrock beneath the soil) due to extreme heating followed by rapid cooling. Temperatures at the base of a large wildfire can exceed 1000 °C (Wotton et al., 2012). The potential increase in transmissivity between the surface and cave caused by fracturing could reduce the concentration of bedrock-derived elements dissolved in dripwaters. Furthermore, the conversion of limestone into lime (CaO) at high temperatures (> 900 °C, Moropoulou et al., 2001) can occur, which may increase meso-porosity (pore widths between 2–50 nm) and macro-porosity (pore widths > 50 nm) while decreasing micro-porosity (pore widths < 2 nm) of the calcined rock (Rouquerol et al., 1994; Valverde et al., 2015; Wang et al., 2019). When lime is subsequently mixed with water (e.g. rainwater), the most reactive CaO particles dissolve first, potentially increasing both pH and supersaturation relative to calcium carbonate (Kemperl and Macek, 2009; Hartland et al., 2010). This could enhance calcium carbonate precipitation within the cave, and thus promote speleothem extension rate. Post-fire impacts on speleothem extension rate could be further augmented by an increase in infiltration and drip rate due to loss of vegetation (Genty and Quinif, 1996; Nagra et al., 2016; Weber et al., 2018).

Speleothems from shallow caves are potentially ideal archives for studying the impacts of fires as confounding factors such as long infiltration pathways, lag times and the mixing of stored water with post-fire infiltration are minimised (Bian et al., 2019). Yonderup Cave in Yanchep National Park (YNP), south-west Western Australia (WA), is a shallow cave (6 m depth) in a region impacted by wildfires. An environmentally significant trace element record was previously produced from a stalagmite (YD-S2) in Yonderup Cave spanning the 20th century (Nagra et al., 2017). Stalagmite YD-S2 was fed by an actively dripping stalactite before its removal and commencement of dripwater monitoring in July 2005 (Nagra et al., 2016, Site 1a). A hydrochemical response in the properties of cave dripwater was detected following a fire event that occurred whilst the cave was being monitored (Nagra et al., 2016). This suggests that Yonderup Cave is ideal for examining changes in speleothem geochemical composition caused by wildfires. Here, we identify the geochemical 'fingerprint' of a fire event by comparing the speleothem geochemical record with the known fire history and extend this information to construct a 245-year record of paleo-fire events. Our improved record from YD-S2 is developed using annual lamina counts obtained from 2D elemental and physical maps, and includes new chemical parameters: bromine (Br), sulphur (S) and colloidal material.

2. GEOLOGIC, CLIMATIC AND HISTORICAL SETTING

The ceiling above stalagmite YD-S2 is located approximately 4 m below the ground surface in Yonderup Cave, overlying a chamber that is approximately 7 m in height (Nagra et al., 2016). 70% of the ground cover above the YD-S2 site has an average soil thickness of 124 mm with the other 30% covered by exposed bedrock (Nagra et al., 2016). Yonderup Cave is located approximately 47 kilometres north-northwest of Perth in YNP, Western Australia, and approximately 6.5 kilometers from the coast (Fig. 1). The cave developed in the Tamala Limestone lithostratigraphic unit, an extensive Pleistocene aeolianite,
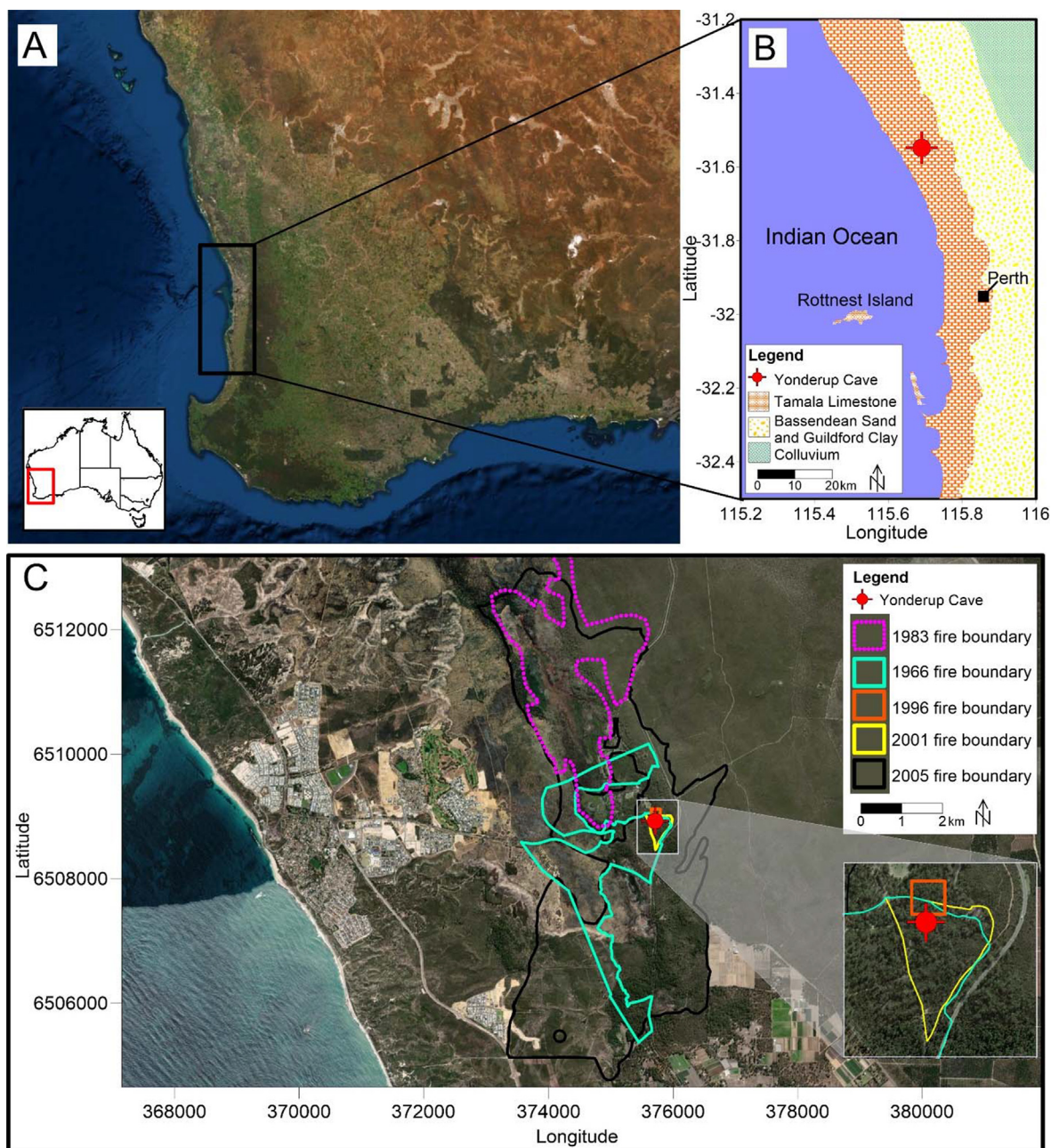

Fig. 1. A) Map of the study region with B) inset showing the location of Yonderup Cave and extent of the Tamala Limestone (adapted from Smith et al., 2012). Coordinates are shown as WGS84. C) Maps of fire extent for fires which burned over the top or in close vicinity (< 10 m) of Yonderup Cave in 1966 CE, 1996 CE, 2011 CE, and 2005 CE (Department of Biodiversity, Conservation and Attractions, 2020). The approximate boundary of an additional fire observed in satellite imagery (Fig. S1) in 1983 is shown as a dotted pink polygon. Coordinates are shown in WGS84 Zone 50S. N.B: large fires occurring in Yanchep National Park in 1977 CE (500 ha burnt) and 1983 CE (800 ha burnt) are reported in Department of Environment and Conservation (2010) but are not available as shapefiles. The positioning of YD-S2 within the cave is provided in Nagra et al. (2016).

outcropping along the coast of southwest Western Australia (Playford et al., 1976; Playford et al., 2013). The Tamala Limestone is an aeolian calcarenite (aeolianite), comprised predominantly of carbonate bioclasts and quartz grains, with a smaller amount of feldspar and subordinate interbedded microbialite (Lipar and Webb, 2014). The carbonate bioclasts of the aeolianite originally consisted of high magnesium (Mg) calcite and aragonite, both of which commonly transform into low-Mg calcite with diagenesis. In this process, cave development must have proceeded contemporaneously with the lithification of the aeolianite into a limestone (eogenetic karst). Thus, although meteoric diagenesis of the Tamala Limestone may have resulted in a dual porosity system consisting in many connected channels within a matrix of interparticle pores, which engender a diffuse, dispersive flow, the formation of caves suggests that rapid conduit flow and rapid transmissivity from the surface to the underground occurred (Smith et al., 2012). The meteoric diagenesis of the carbonate component of the aeolian calcarenites of the Tamala Limestone show a progressive reduction in aragonite and high-Mg calcite content (through dissolution) with increasing age (depth), and a corresponding increase in low-Mg calcite content (through re-precipitation). Bryan et al. (2017) actually identified an excess of Mg in groundwaters that interacted with Tamala Limestone, and attributed this to ongoing diagenesis of unstable Mg-calcite. Thus, whilst Sr may be derived from both aragonite or silicate dissolution, any contribution of host rock Mg most likely derives primarily from Mg-carbonates.

2.1. Climate characteristics, vegetation and fire-history

The climate at Yanchep is classified as Mediterranean (Köppen climate classification Csa; Beck et al., 2018) with hot, dry summers and cool, wet winters. The Australian Bureau of Meteorology manages a weather station (number 009053) located approximately 33 km south-east of the study site, which has recorded long-term temperature (1937–2020 CE) and precipitation (1937–2020 CE) data. The long-term average rainfall rate is 652 mm year^{-1} (minimum = 348 mm year^{-1}, maximum = 985 mm year^{-1}), with most (56%) of the rain falling during winter, an intermediate amount in autumn and spring (20% and 19% respectively), and a small proportion (5%) falling during summer. The long-term average maximum and minimum temperatures are 25.3 ± 1.4 °C (1 σ) and 12.4 ± 1.0 °C (1 σ).

Pre-European vegetation near the cave area is classified as low forest and woodland (< 10 m tall) consisting of wattle, banksia, peppermint, cypress pine, casuarina and York gum (Beard et al., 2013). Areas of medium forest woodland (10–30 m tall), scrub heath and thicket were present to the west of the caves towards the coast (Beard et al., 2013). Current vegetation consists of tuart (*Eucalyptus gomphocephalla*) forest, banksia heath and wetland vegetation.

The Yanchep region is prone to the occurrence of wildfires in summer due to the combination of low rainfall, frequent lightning storms and abrupt wind changes caused by pre-frontal troughs (McCaw et al., 2003). A number of fire events in the recent past within the bounds of the YD-S2 record are known to have occurred at YNP. These include three prescribed burns above or in very close proximity (< 10 m) to Yonderup Cave in 1966 CE, 1996 CE and 2001 CE (Fig. 1, Nagra et al., 2017). A wildfire in 2005 CE also burnt directly over the cave approximately 6 months prior to the collection of YD-S2 (Fig. 1). Two other wildfires are also reported to have occurred in the broader YNP region in 1977 CE and 1983 CE and burnt 500 ha and 800 ha respectively (Department of Environment and Conservation, 2010). Satellite imagery reveals that the 1983 CE fire burnt to the north-west of the cave (Figs. 1 and S1). Imagery for the 1977 CE event is unavailable, and it is unclear whether this fire burned directly over the cave.

2.2. Indigenous and European history

Traditionally, Yanchep was a meeting place for the Noongar people prior to European colonisation. It was chosen for its proximity to the coast, lake, forest and wetland areas, which contained abundant resources. The area has mythological, ritual and ceremonial significance for the continent's First People (Department of Conservation and Land Management, 1989). The first documented account of Europeans visiting Yanchep was in 1834 CE (Department of Conservation and Land Management, 1989). In 1835 CE a stock route was established and used by drovers however the Yanchep area was not settled by Europeans until 1901 CE (Department of Conservation and Land Management, 1989). Most of the caves in YNP were explored by Europeans shortly thereafter in 1904 CE (Department of Conservation and Land Management, 1989). In 1932 CE Yonderup Cave was officially opened to the public as a tourist attraction, and tours began. Historical photos of when the cave was discovered show that the original entrance was not substantially different in size compared with the current entrance, hence we do not expect that artificial modification to the entrance would have significantly altered the cave microclimate.

3. METHODS

Stalagmite YD-S2 was analysed through synchrotron based micro x-ray fluorescence (SR-XRF) elemental mapping, excimer laser ablation inductively-coupled plasma mass spectrometry (LA-ICPMS), thin section observations for calcite fabric and colloidal particulates (including OM) and stable isotope ratios (δ^{13}C, δ^{18}O) mass spectrometry. YD-S2 was sectioned in half along its central growth axis using a 2 mm wide diamond blade. One half was sectioned along the growth axis to produce adjacent slabs for both stable isotope ratios and elemental analyses. SR-XRF and LA-ICPMS were conducted on the same polished slab and the thin section was cut from the back of this slab. The presence of laminae visible to the naked eye permitted verification that sampling depth was comparable across the sub-sampled pieces for different analytical techniques. Details for the methods are provided below.

3.1. Synchrotron micro X-ray fluorescence (SR-XRF)

SR-XRF elemental mapping of calcium (Ca), bromine (Br), strontium (Sr) and zinc (Zn) was undertaken at The Australian Synchrotron, Australian Nuclear Science and Technology Organisation (ANSTO) in Melbourne at a 2 µm resolution using a monochromatic incident beam with energy of 18.5 keV. The beam was focused to a spot size of 1.5 µm on the sample, and a dwell per pixel from 1 to 4 milliseconds (ms) was used. Data were collected using the Maia 384 (Sync) – HYMOD detector and then reduced through the CSIRO Dynamic Analysis method and GeoPIXE software. Counts were analysed to obtain true-elemental images in absolute values as micrograms per gram (µg g^{-1}) (Ryan et al., 1995; Ryan et al., 2005). ImageJ (https://imagej.nih.gov/ij/) was then used to extract time-series of absolute concentrations at 2 µm intervals perpendicular to the growth laminae using a 20-pixel line width. A 13-point (0.24 µm) Savitzky-Golay filter was applied to the Br map to reduce noise in the dataset that could obscure the long-term trends, whilst also preserving the peaks and troughs. This method fits successive time frames (windows) with a polynomial via linear least squares in order to reduce high frequency noise (Savitzky and Golay, 1964). In particular, the use of a small window size (0.24 µm) ensures that seasonal signals are maintained. This method is commonly used to smooth timeseries data in paleo-environmental studies (e.g. Baldini et al., 2008; Nagra et al., 2017; Ban et al., 2018; Faraji et al., 2021).

The SR-XRF elemental maps of light elements (S, Mg and P) were recorded at beamline 10.3.2 (Marcus et al., 2004) of the Advanced Light Source (Lawrence Berkeley National Laboratory, Berkeley, California, USA) using a 10 × 10 µm pixel size, a 200 ms dwell time/pixel, an incident photon energy of 3988 eV (50 eV below the Ca K-edge) and a beam spot size of 7 × 7 µm. The maps were recorded with an Amptek FAST XR-100SDD C2 single element detector. Maps were then deadtime corrected and extracted with LabVIEW software available at the beamline. A collapsed line plot of the scan was obtained from ImageJ using a line width of 20 and relative concentrations at 10 µm intervals were exported to excel. Absolute concentrations could not be determined for P, Mg and S owing to a lack of matrix-matched standards at the time of these measurements.

3.2. LA-ICPMS trace element data

Trace element data were previously published in Nagra et al. (2017). In this previous publication, two datasets were considered: a 'high' and a 'low' resolution dataset acquired by masking the laser to a 5x35 micron slit and 32 micron circle, respectively. The upper 12.15 mm of YD-S2 lower resolution data were used for the reconstruction in their Fig. 5, whereas a total of 18.87 mm of data were analysed and are presented in full here. Aluminium (Al), barium (Ba), uranium (U), zinc (Zn), copper (Cu), lead (Pb), phosphorus (P), magnesium (Mg) and strontium (Sr) elemental data were analysed using excimer laser ablation inductively-coupled plasma mass spectrometry (LA-ICPMS) at The Australian National University (ANU).

The method is reported in Nagra et al. (2017) and briefly summarised here. Full description of the procedure for LA-ICPMS of speleothems at ANU are given in Treble et al. (2003). The laser system consists of a LambdaPhysik LPX 120i ArF excimer with a wavelength of 193 nm coupled to an Agilent 7500 s quadrupole ICP MS. A motorised stage was used to acquire data in continuous scanning mode at 2 mm min^{-1} with laser firing at 12 Hz and masked to a 32 µm circular spot. The ICPMS was tuned to maximise sensitivity between the lower and mid-range of masses analysed. Five parallel tracks were acquired over a maximum lateral spacing of 1 mm. Background subtraction and linear drift correction were applied to raw count rates and ratioed to Ca count rates after the Ca had been pre-treated with a 3-point box smooth to remove transient spikes. Metal/Ca count ratios were converted to concentration using NIST SRM612 except for P and U for which NIST SRM614 was used (concentrations given in Nagra et al., 2017). Metal timeseries were cross-checked with Ca count rates (e.g., Fig. S2) to eliminate the possibility of apparent peaks in metals concentrations due to decreases in Ca count rates which can occur when the laser passes over cracks or porous sections of the calcite surface (Borsato et al., 2021). To assess lateral consistency of features in metal concentrations, timeseries of five tracks of Al are shown in Fig. S3. LA-ICPMS data were also compared to synchrotron data and observed to show more clearly defined peaks and troughs compared to the synchrotron line scans obtained from ImageJ for P, Mg and Sr. Therefore, the LA-ICPMS data was selected for use in the principal component analysis (PCA) for these elements over the line plots obtained from the synchrotron scans. A comparison of the synchrotron and LA-ICPMS results is shown in Fig. S4. Data output by ICPMS is determined by the ICPMS measurement cycle thus the time stamp was converted to distance according to the length of the sample scanned yielding an apparent sampling resolution of 6.3 µm, although the laser was masked to 32 µm Section 3.2.

3.3. Stalagmite fabrics and colloidal organic matter

Fabrics, which refer to the spatial arrangement of crystals in the stalagmite, were observed via optical microscopy on 30 µm thick thin sections using a Zeiss Axioplan and Leica MS16 stereomicroscope in transmission light mode at the Speleothem Microscopy Laboratory of the University of Newcastle, Australia. Fabrics were described and coded following a conceptual framework that reflects changes in the cave environmental parameters (Frisia, 2015). The entire thin sections were imaged using a flatbed scanner Epson Perfection V550 with a resolution of 2540 dpi, which is sensitive to fabric changes such as porosity and impurities as determined by optical microscopy in transmission mode. In plane polarized optical microscopy mode, overall porosity results in the observation of "white" holes when pores are empty, whilst when pores are filled by impurities they result in the "dark" particles. If these particles are < 2 µm in diameter, they are labelled colloid or particulate. Pores can also be filled by water, which would still

yield a "light" contrast. In the greyscale, relative colloidal concentrations were extracted from the thin section scan using ImageJ, whereby darker brown bands (low greyscale) represent higher colloidal material incorporated into the speleothem. Please note that here we insist on "speleothem" incorporation and not in "calcite", which is the crystalline phase that builds up the stalagmite. These values were inverted by subtracting each value from 250 to display high values as relatively high relative colloidal concentrations. The extraction of the greyscale values was performed in ImageJ along the growth axis (perpendicular to the lamination). Where cracks in the thin section lamina were present, these occurred diagonally (most likely following calcite cleavage planes), therefore the corresponding values were extracted along parallel lines on the right or left side of the master line, in order to avoid the damaged area. We note that whilst OM is referred to as colloids and metals as ions throughout the manuscript, metals are typically bound to and transported via organic matter colloids into cave systems (Hartland et al., 2011; Hartland et al., 2012). As such the presence, patterns and behaviours of metals are interpreted following the principles of colloid transport.

3.4. Stable isotope ratios

Speleothem $\delta^{18}O$ and $\delta^{13}C$ were analysed at the Research School of Earth Sciences, ANU. Powders were continuously milled along the edge of the growth axis using a 2 mm diameter tungsten carbide end-mill bit, effectively shaving samples at 0.1 mm increments, following the method of Gagan et al. (1994). A 'clear cut' was made at each increment by milling an additional 1 mm into the sample to account for the curvature of the bit before cutting the next sample. 180–220 μg samples were weighed and analysed using a Finnigan MAT-251 dual-inlet stable-isotope ratio mass spectrometer coupled to a Kiel I micro-carbonate preparation device. The measured delta values were aligned to the VPDB scale using the National Bureau of Standards NBS-19 standard ($\delta^{18}O_{VPDB} = -2.20\permil$ and $\delta^{13}C_{VPDB} = +1.95\permil$). A further linear correction for $\delta^{18}O$ was made using the NBS-18 standard ($\delta^{18}O_{VPDB} = -23.0\permil$). This minor scaling adjustment changes the measured $\delta^{18}O$ values by no more than $0.03\permil$ over the range of $\delta^{18}O$ for YD-S2 (-2 to $-5\permil$). The original delta values for NBS-19 and NBS-18 are used to maintain consistency of results through time in the RSES Stable Isotope Laboratory. No scaling adjustment is required for measurements of $\delta^{13}C$ over the range of values for YD-S2 (-2 to $-8\permil$). Analytical precision for repeat measurements of NBS-19 run in parallel with the stalagmite samples was $0.04\permil$ for $\delta^{18}O$ and $0.02\permil$ for $\delta^{13}C$ (1σ, n = 34).

3.5. Chronology

A chronology for YD-S2 (0–12.15 mm distance from top; DFT) was already obtained by Nagra et al. (2017) by using LA-ICPMS line scans. In the dataset presented here (covering 0–18.87 mm DFT), the clearest laminae information was visible in the thin section and in the synchrotron map for Sr concentrations (Fig. S5). Accordingly, laminae counting and error estimate in this study were carried out primarily by determining the position of the OM-rich laminae on thin section images at six confidence levels ($> 95\%$, $75–95\%$, $50–75\%$, $25–50\%$, $5–25\%$, and $< 5\%$ confidence) using ImageJ software package (Faraji, et al., 2021) in the region of 0 mm–18.87 mm DFT. Where the laminae were clear and easily visible, a confidence level of $> 95\%$ was assigned with no associated error applied. Where a lamina appeared very blurry or unclear, a corresponding confidence level 0–5% was assigned. These thin section laminae were verified against the Sr SR-XRF maps, and for a few laminae ($< 5\%$ of the total laminae across the 18.87 mm area of interest), Sr bands were used as the primary counting method due to low amounts of colloidal material. The calculated error is up to 13 years for 1760 CE to 1887 CE, and up to 4 years for 1888 CE to 2005 CE.

U-Th dating of YD-S2 was also undertaken at the Radiogenic Isotope Laboratory, The University of Queensland. U-Th dating of low-U speleothem samples with only a few hundred years of age is analytically challenging due to the presence of extremely low radiogenic ^{230}Th. In this study, sub-samples weighing 145–175 mg were spiked with a ^{233}U-^{229}Th mixed tracer, digested with double-distilled HNO_3, chemically separated and purified using THRU-spec resin and measured on a Nu Plasma HR multi-collector inductively-coupled plasma mass spectrometry (MC-ICP-MS), adopting an analytical protocol recently modified after Zhou et al. (2011) and Clark et al. (2014). Rather than using the two-sequence peak jumping mode for acquisition of U-Th isotopes as previously described, to improve analytical efficiency and precision for analytically challenging young samples, we adopted a single-sequence static mode whereby ^{238}U, ^{235}U, ^{233}U, ^{232}Th and ^{229}Th isotopes were measured on the Faraday cups and the low-abundance ^{234}U and ^{230}Th isotopes collected on the two parallel multipliers separated by four mass units. A standard-sample-standard bracketing approach was used to normalize the isotope ratios of the unknown samples to those of the monitoring standard. The instrument sensitivity was also optimized using a modified sample-skimmer cone set. As a result, we achieved analytical precisions of $\sim 2–3\%$ for the $^{230}Th/^{238}U$ activity ratios with ^{230}Th signals ranging from only 12–18 counts/second in the three sub-samples of only 145–175 mg in weight and 0.1–0.12 μg g^{-1} in U concentration. As the dated sub-samples contain a fair amount of detrital Th as reflected by their elevated ^{232}Th levels or low measured $^{230}Th/^{232}Th$ activity ratios, we applied detrital or non-radiogenic ^{230}Th correction assuming an initial $^{230}Th/^{232}Th$ activity of $1.14 \pm 20\%$. As a result, the corrected ^{230}Th ages overlap completely within their 2 standard deviations with the dates independently identified by the lamina counting of 1785 ± 27, 1823 ± 22 and 1870 ± 13 for YDS2_UQ04, YDS2_UQ05 and YDS2_UQ06, respectively.

3.6. Statistical analysis

Shapiro-Wilk's tests for normality were performed in RStudio (v.1.1.456) on individual variables. All variables returned a p value > 0.05 suggesting that the distributions

are significantly different from normal. Non-parametric Spearman's correlations were therefore used to assess correlations between variables in the results section. The mean peaks in P pre- and post-1900 CE were compared using a two-sample t-test assuming unequal variances.

Change-points in the mean and variance of the data were examined with RStudio (v.1.1.456) changepoint package using a binary segmentation method (Scott and Knott, 1974) and pruned exact linear time (PELT) method (Killick et al., 2012). The PELT method reportedly has increased accuracy relative to other change-point identification methods (Killick et al., 2012), however it was only suitable for assessing Mg variability. For the other time-series it resulted in an identification of almost all values as change-points. In these instances, the binary segmentation method was used.

PCA was conducted to determine the main processes affecting the elemental, colloid/OM and stable isotope composition of YD-S2. PCA allows for the detection of relationships between variables through dimensionality reduction. Orthogonal linear combinations of variables explaining the most variability in the data are called principal components (PCs, Lansangan and Barrios, 2009). Each PC explains a proportion of the total variability observed in the data. For each PC, variables are assigned a loading between −1 and 1 which describes the correlation of the variable with the PC. For example, a variable score close to −1 or 1 indicates a very good negative or positive correlation, meaning that the PC of interest explains a good amount of the variability in the dataset for that parameter. A score of close to 0 suggests that the parameter does not contribute much to the PC of interest. For this reason, a variable with a score close to 0 on a component of a time-series PCA should not be heavily interpreted with respect to the trends displayed by that PC. PCA techniques have previously been used in other studies to identify underlying forcing mechanisms affecting trace elements in speleothems (Orland et al., 2014; Nagra et al., 2017). We undertook PCA to gain insight on what climatic conditions lead to wildfires and to obtain information on environmental changes brought about by fires during known fire events. These changes are then linked to observations in the pre-instrumental record. PCA was performed on the YD-S2 time-series data using data interpolated to the high-resolution LA-ICPMS data as the trace element data contain many short-lived peaks that are of interest to this study are not represented when the high resolution LA-ICPMS trace element data are interpolated to the lower resolution of the stable isotope data. To do this, the colloid/OM and SR-XRF Br and S time-series were obtained from thin section and SR-XRF maps respectively after processing in ImageJ. Data were linearly interpolated in OriginPro v.9.7.5.184. PCA was then performed in Python using *sklearn.decomposition.PCA*, with the loadings of each parameter on the leading principal components, and changes in the principal component values over time assessed.

Biplots were generated in RStudio (v.1.1.456) using the PCA() and fviz_pca() functions of the FactoMineR (Lê et al., 2008) and factoextra (Kassambara and Mundt, 2020) packages. Groups are based on k-means using the loadings of each variable on the PCA components, whereby variables are assigned to a cluster based on Euclidean distances between the variable and the closest cluster centroid. Variables within the same cluster have high intra-class similarity of loadings on the PCA components. We note that there is no discrepancy between the PCA results using the R functions and the PCA generated in Python.

4. RESULTS

4.1. Chronology

The upper 18.87 mm of stalagmite YD-S2 contains visible, flat and parallel laminae over a width of at least 20 mm. Darker bands in the thin section indicate relatively higher colloid concentration in the wet season. These likely consist of OM as shallow cave depths result in low to negligible OM filtering effects (cf. Frisia and Borsato, 2010) (Fig. S6). Alternating dark and light bands coincide with low and high Sr concentrations respectively, demonstrating that a higher proportion of colloids/OM incorporated into the speleothem is associated with its low incorporation of Sr, as documented in other shallow caves (Borsato et al., 2007). The observed relation between dark, OM-rich layers and low Sr concentration points to pH and supersaturation state control of low calcite deposition during the wet season (Frisia et al., 2000). This is further confirmed through a negative relationship between growth rate and Sr concentration (p < 2.2 × 10^{-6}, r$_s$ = −0.22). We also observe a negative correlation between growth rate and S concentration (p < 2.2 × 10^{-6}, r$_s$ = −0.19). Seasonal ventilation in winter results promotes dripwater CO_2 degassing, resulting in an increase in pH and calcite saturation state, leading to bicarbonate competition for space within the lattice and reduced S incorporation (Wynn et al., 2018). The appearance of seasonal colloidal particulates in YD-S2 is consistent with highly seasonal recharge and a short flow path length implying relatively fast transmission from the soil zone.

A total of 246 ± 12 annual layers were counted in the upper 18.87 mm of YD-S2. This results in an age span from 1760 ± 13 CE to the known collection date of July 14th, 2005 CE at 0 mm DFT (Fig. 2). Complex stratigraphy below 18.87 mm prevents the interpretation of the earlier YD-S2 paleo-environmental record. Fig. 2 shows the new age-depth model against the Nagra et al. (2017) age-depth model. The identification of laminae in two-dimensions using the thin section and synchrotron maps reduces uncertainties intrinsic to the LA-ICPMS peak-counting method (Nagra et al., 2017) and produces more robust chronologies in stalagmites where radiometric dating can be problematic (Faraji, et al., 2021; and see Supplementary Note 1 for further information). U-Th dates are shown in Table S1 and suggest that there are no extended hiatuses through the YD-S2 record, providing further validation of the lamina counting chronology.

The new age/depth model shows a prominent change in vertical extension rate of the stalagmite after 935 um (1897 CE) supported by change point analysis (Fig. S7, see Baker et al., 2021). The average annual vertical axis extension rate

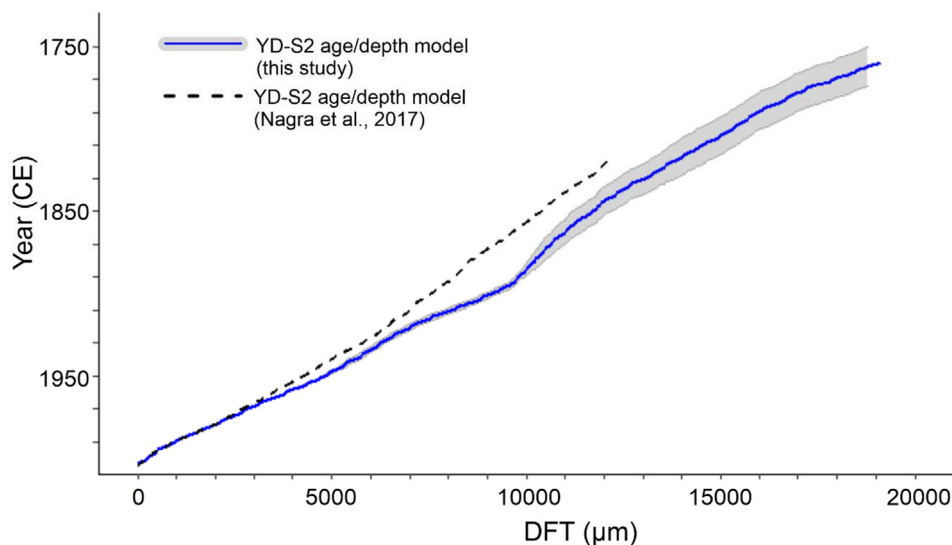Fig. 2. Chronology of YD-S2 based on lamina counts. Lamina age (Year CE) is shown on y-axis and distance from the top (DFT μm) of the speleothem shown on the x-axis. Grey shading shows the envelope of uncertainty for the lamina counts. Black dashed line represents the chronology as reported in Nagra et al. (2017).

for YD-S2 is 86 ± 27 μm yr^{-1} (1σ, Table S2). Change-point analysis shows a high mean extension rate occurred in 1760–1775 CE (116 ± 26 μm yr^{-1}, 1σ). The rate decreases between 1775–1854 CE (72 ± 23 μm yr^{-1}, 1σ) (Fig. S7, Table S3) and then drops to the lowest rate observed in the data between 1854 and 1896 CE (44 ± 23 μm yr^{-1}, 1σ). A pronounced long-term shift to higher extension rates occurs after 1896 CE (Fig. S7, Table S3) and declines after 1995 CE.

4.2. Chemical properties: $\delta^{18}O$, $\delta^{13}C$, minor and trace element concentrations

There is a strong correlation between $\delta^{18}O$ and $\delta^{13}C$ values for the entire dataset ($r_s = 0.85$, $p < 0.001$), which is weaker during the period 1900–1940 CE ($r_s = 0.52$, $p < 0.001$) (Fig. S8). A positive correlation between $\delta^{18}O$ and other variables: Mg ($r_s = 0.56$, $p < 2.2 \times 10^{-16}$), $\delta^{13}C$ ($r_s = 0.72$, $p < 0.001$) and Br ($r_s = 0.54$, $p < 0.001$) is observed. These have higher mean values during the late 1820s-1830s CE and again during the 1860s-1890s CE, followed by an abrupt shift to lower mean values from 1897 CE ($\delta^{18}O$, $\delta^{13}C$ and Mg) and 1911 CE (Br) as supported by change point analyses (Table S3). Additionally, Mg and stable isotopes ($\delta^{18}O$ and $\delta^{13}C$) display a short-lived maxima at 1897 CE during or immediately after the occurrence of a large peak in P concentration (Fig. 3).

The large peak in P in the LA-ICPMS data (Fig. 3) is also evident in the SR-XRF P map in Fig. 4 as a continuous lateral feature coincident with a depletion in S, and peak concentrations in Mg and Sr. This significant "layer event" appears to occur during the dry season, where the laminae in the thin section are lighter due to reduced colloid/OM incorporation (Fig. S6). The 1897 CE event is also clearly visible as a peak in PC3 in the historical record (Fig. 5) and is associated with an increase in Zn concentrations

which last for approximately 1 year (Fig. 6). Increases in Cu, Al and Pb concentrations are not observed during this event.

Significant correlations ($p < 0.001$) are observed between Ba and U ($r_s = 0.61$), Ba and S ($r_s = 0.74$), S and U ($r_s = 0.56$), Sr and S ($r_s = 0.66$) and Sr and Ba ($r_s = 0.62$) (Table S4). Fig. 3 shows that S and Ba mean concentrations increase from approximately 1870 CE to the mid-1880s CE. Concentrations of both elements rapidly drop in the mid 1880s CE, approximately 11 years prior to the peak in P in 1897 CE (Fig. S7, Table S3). Change-point analysis indicate that Ba, Sr and S mean concentrations began to rise again after the mid to late-1980s CE. Change-points in the mean were not detected in the U data, likely due to high variability in the dataset.

4.3. Principal component analysis

PCA and k-mean clustering (Table S5) was undertaken on all variables to gain insight on climatic conditions and other environmental information contained in this speleothem record (Fig. 5). Overall, PC1, PC2 and PC3 explain 34.1%, 17.7% and 11.8% of the variation in the dataset respectively. The interpolation of the lower resolution stable isotope data ($\delta^{13}C$ and $\delta^{18}O$, 100 μm intervals) to higher resolution (6.3 μm intervals) did not impact our interpretation of trends on PC1 and PC2 (Fig. S9). Furthermore, the exclusion of metals and the 1897 CE event from the low resolution PCA results in greater percent variance explained on PC1 and PC2 (46.7% and 19.2% respectively) but does not change the observed long-term trends on either component (Fig. S9).

Variables Mg, Ba, $\delta^{13}C$, $\delta^{18}O$, Br, U and colloids/OM load most strongly on PC1 (Fig. 5B; Table S6), whereas S loads most strongly on PC2. The Sr loading is relatively evenly spread between PC1 and PC2, while P loads most
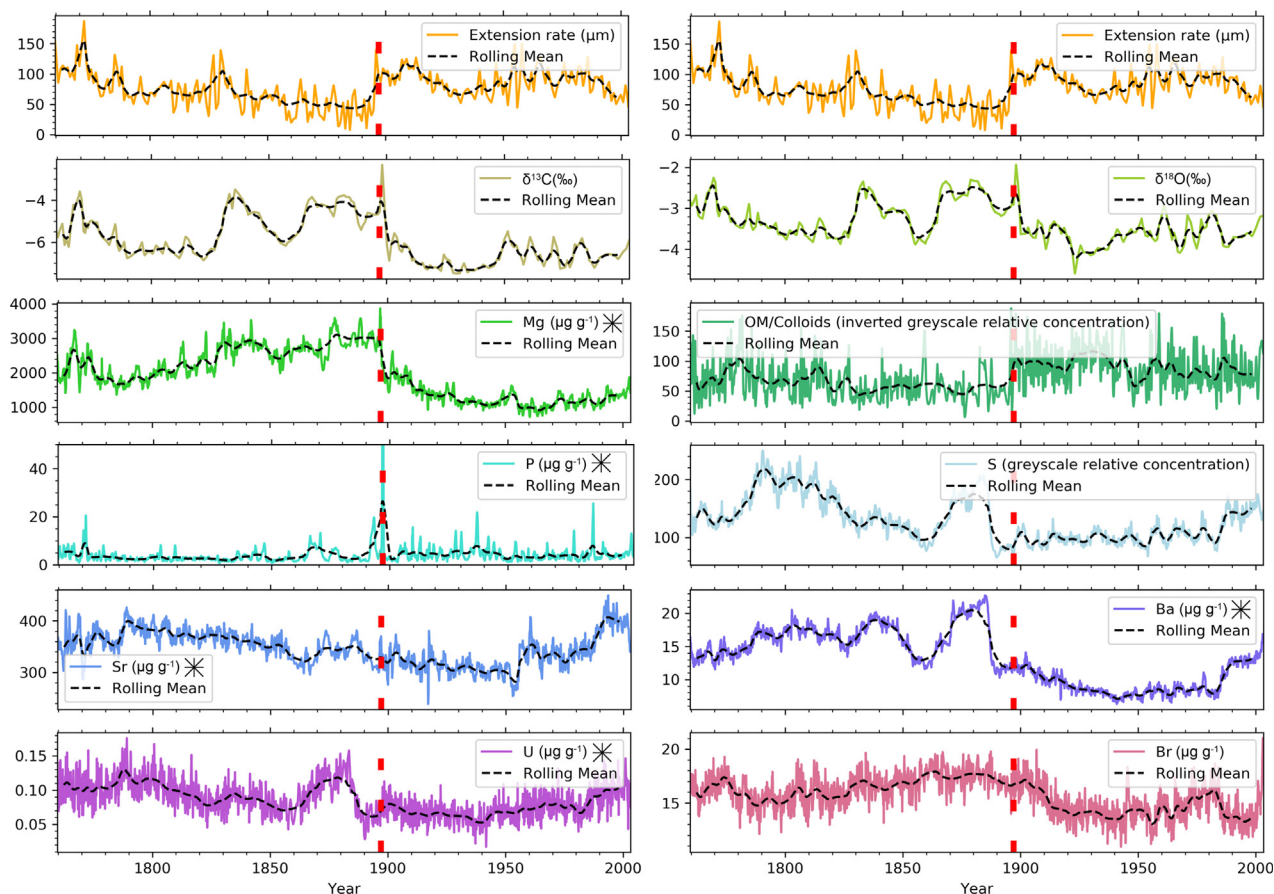
Fig. 3. Time-series of extension rate (top panel) and geochemical variables included in the PCA. Extension rate is duplicated in the top panel for easy comparison between extension rate and parameters. The y-axis on the phosphorus (P) timeseries plot is limited to 50 μg g^{-1} for increased visibility of P peaks through the record (maximum value at 1897 CE is 161 μg g^{-1}). The 1897 CE event is marked by a red dashed line. The black dashed lines represent an approximately 5-year (window size = 100) rolling mean concentration. Variables measured by LA-ICPMS are indicated by a black asterisk in the legend. Sulfur (S) and bromine (Br) are measured by SR-XRF.

strongly on PC2 and PC3, with very little variability in P explained by PC1. Metals Al, Cu, Zn and Pb, all load most strongly on PC3 which is dominated by fewer, large peaks and often associated with P.

PC3 shows high variability and largely represents peaks in metal concentrations within the stalagmite, as indicated by their strong loading on PC3 (Table S6). Peaks in PC3 were assessed to determine whether these align with known fire events in the modern record (Section 2.1). The biplot shown in Fig. 5B strongly points to a soil, vegetation or ash source of trace metals (Al, Cu, Zn and Pb), as they cluster with P and colloids/OM.

Peaks in PC3 are classified as values exceeding the rolling median PC3 value (window size = 40) by 2.5 times the rolling standard deviation (blue bars in Fig. 6). A comparison of peak identification methods is provided in Table S7. Fig. 6 confirms that four of the five known modern fire events (1966, 1977, 1996 and 2001) coincide with peaks in PC3, aside from the 1983 CE fire. There are two blue bars in the modern period (1974 and 1990 CE) that do not coincide with known fires and this is discussed further in

Section 5.1. Pb, Zn and Al load most strongly on PC3 (each explaining ≥ 15% of the variability on PC3) suggesting these parameters may be the most useful for identifying fire events in the stalagmite.

Fig. 6 also shows peaks in PC3 in the YD-S2 record prior to modern fire record. These indicate possible fire events in the years 1762, 1766, 1769, 1773, 1782, 1787, 1813, 1817, 1820, 1823, 1863, 1871, 1897, 1902, 1917, 1931, 1942, 1946 and 1958 CE. Each of these peaks is associated with a spike in P, Zn, Al, Cu, and/or Pb. The highest P concentration (161 μg g^{-1}) in the record is observed in 1897 ± 5 CE. Aside from this event, P concentrations during identified peaks in PC3 are significantly lower (p = 0.02) and less variable (average = 4.0, variance = 1.9, n = 10) in the pre-1850 CE period than in the post-1900 CE period (mean = 6.3, variance = 11.5, n = 12).

4.4. The 1897 ± 5 CE "event"

A sudden shift in the vertical extension rate at 9.45 mm DFT (1897 ± 5 CE) closely coincides with a change in mean
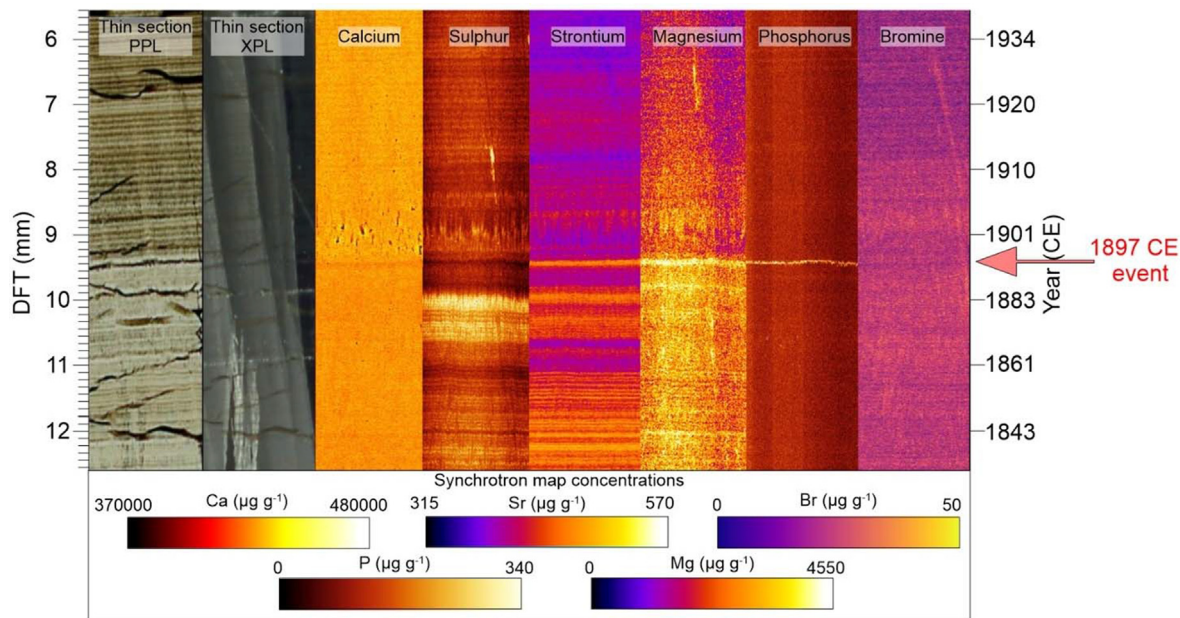
Fig. 4. Thin section parallel-polar image (PPL), cross-polar image (XPL), and synchrotron SR-XRF maps for calcium, sulphur, strontium, magnesium, phosphorus and bromine. The 1897 CE event is associated with a micro-hiatus in the PPL image, a strong peak in P and smaller peaks in Mg and Sr. The post 1897 CE period is characterised by higher colloidal/OM concentrations, a decline in Mg and Sr, and an increase in the calcite porosity evident in the Ca map. Ca, Sr and Br maps were recorded at the Australian Synchrotron, S, Mg and P maps were recorded at the Advanced Light Source, Berkeley Lab, USA. Matrix-matched standards were not available at the time of measurement to obtain absolute concentrations for Mg, P and S. As P and Mg were measured by LA-ICPMS, the scale bar concentrations for these elements were calculated based on the LA-ICPMS concentrations.
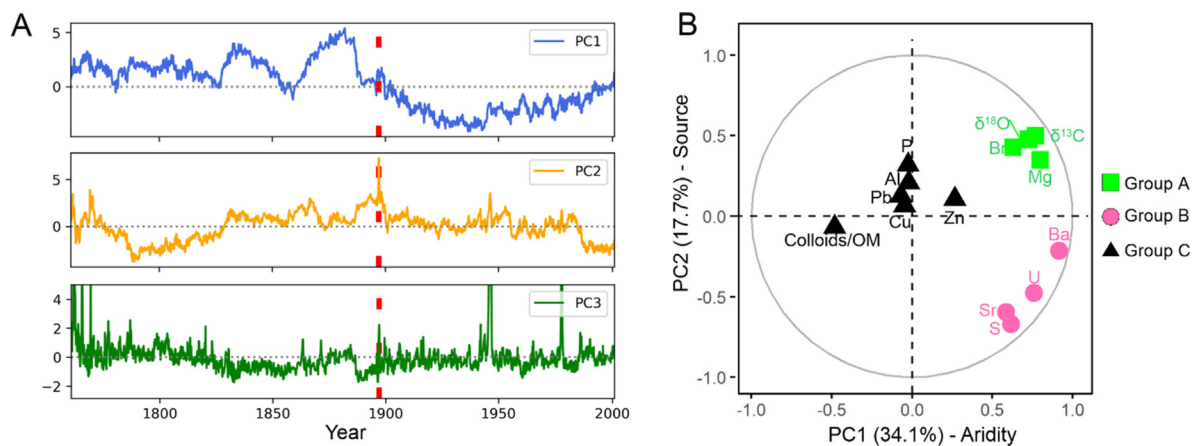

Fig. 5. Time-series using data showing (A) PC1, PC2 and PC3 timeseries. Data has been interpolated to high resolution LA-ICPMS data. PC1 is shown as a blue line, PC2 is shown as a yellow line and PC3 is shown as a green line. The timing of the event at 1897 CE is shown as red vertical dashed line. B) Shows a biplot of the first two principal components. Colours of variables on the biplots show three groupings of variables based on k-means (Table S5), which take into account the relationship of the variables on all components of the PCA.

values for other climate and environmental proxies as follows: i. a maximum in $\delta^{18}O$ and $\delta^{13}C$ in early 1898 CE (-1.9‰ and −2.3‰ respectively); ii. an abrupt peak in Mg concentration (4527 µg g^{-1}) in 1897 CE, followed by a 70% decrease in mean Mg concentrations by 1900 CE that then remain low (Fig. 3, Fig. S7, Table S3); iii. an abrupt increase in the mean relative abundance of colloids/OM in 1897 CE (Table S3), and iv. a clear maximum in P in 1897 CE (Fig. 3), with the value reaching 161 µg g^{-1} (more

than 5 times the median concentration, Table S2), and v. a depletion in S in 1897 CE to the lowest relative concentrations observed through the record.

The fabric during to the 1897 CE event (< 1 year, 9.35–9.45 mm DFT) is defined by a micro-hiatus (see thin section in Fig. 4 and Fig. S5). Optical continuity in crystal growth, no evidence of re-nucleation (accompanied by geometric selection) and no detectable dissolution of crystal tips, as highlighted by the P map (Fig. 4), suggest that this feature
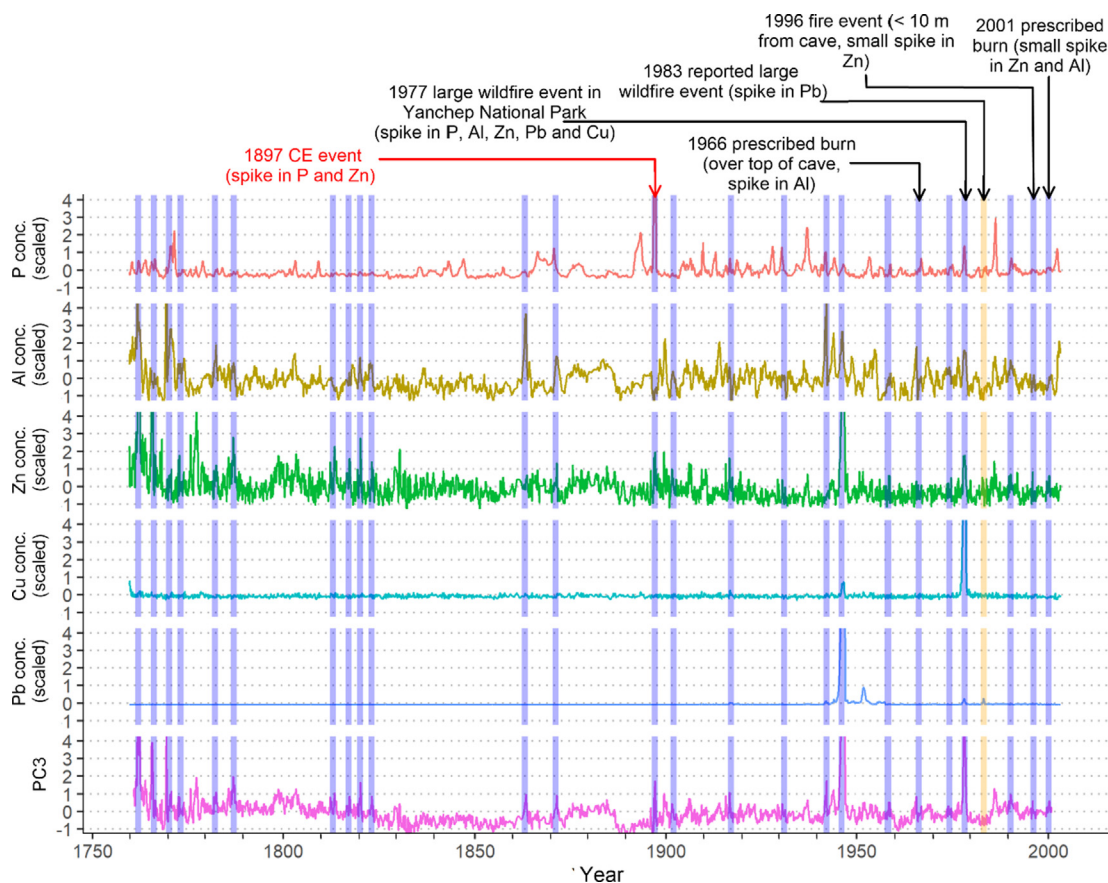
Fig. 6. YD-S2 LA-ICPMS time-series data of centred, scaled soil-derived metal (Cu, Al, Pb and Zn) and P concentrations, and PC3 time-series for the YD-S2 record (main plot). Data is centred and scaled by subtracting the mean and dividing by the standard deviation using the scale() function in RStudio. The y-axis limited to values between −1 and 4 for visual clarity. Blue bands represent points where the rolling median PC3 value exceeds 2.5 times the rolling standard deviation (window size = 40). The yellow band represents a period when another large fire has been reported to have occurred in Yanchep National Park which did not burn over the top of Yonderup Cave. This 1983 event does not show up as a spike on PC3. The shape of the fire scar (Fig. S1) suggests that the wind was likely blowing to the north for this fire event. Fire extent maps are displayed in Fig. 1.

represents a micro-hiatus where cave drips ceased for a short period of time. Above the "micro-hiatus" (i.e. above 9.35 mm DFT) it is evident from the Ca map that the fabric becomes porous (where pores can be either void, or filled by fluid or particulate), with acute crystals tips (clearly visible in the S, Sr and Mg maps) characterized by uniform extinction in Cross Polarized Light (XPL) mode.

5. DISCUSSION

5.1. Validation of fire events in speleothem record

Fig. 6 reveals that whilst PC3 displays short term peaks at most known modern fire events (e.g. 1966 CE, 1977 CE, 1983 CE, 1996 CE, and 2001 CE), the combination of elements that simultaneously increase varies, i.e. implying that the relative loadings of metals on PC3 vary between these peaks. For example, a peak in PC3 values is observed around 1966 CE when a prescribed burn took place above the cave. This peak in PC3 is due to a peak in Al and a peak in P in the following year (9.2 µg g^{-1}). By contrast, the 1977

CE peak in PC3 is due to increases in P, Al, Zn, Pb and Cu (Fig. 6), with the 1977 CE annual averages of P exceeding the 80th percentile of all data (Table S8). Note: Nagra et al. (2017) previously attributed the increase in metals at 1977 as being the result of a heavy rainfall event in 1974 CE, however this improved chronology places this event at the time of the reported 1977 wildfire in YNP with a ± 1 year uncertainty.

The increase in the number of trace metals and their peak concentrations coinciding with the 1977 wildfire versus the 1966 prescribed burn suggests that the suite of trace metals and the magnitude of their response indicate fire intensity. A further example of this is the relatively small response in Zn and Al at the time of the prescribed burn in 2001 CE (Fig. 6). Prescribed burns represent less intense fires (lower combustion temperature, less combustion of vegetation) and would correspondingly have less impact on both soil properties and the amount of ash generated (see Section 5.6 for further discussion on this).

The 1983 CE YNP fire event (Department of Environment and Conservation, 2010) is the only known

modern event that does not appear as a peak in PC3. As the fire did not pass over the top of the cave (Fig. 1), it is possible that significant ash deposition may not have occurred at the surface above YD-S2, particularly as the shape of the fire scar (Fig. 1) indicates that the prevailing wind conditions at the time were away from the cave and thus would not have directed air-borne ash towards the cave. The 2005 CE wildfire which occurred over the top of the cave on January 6th, just over 6 months prior to the stalagmite retrieval, is also not evident in the metal data (Fig. 6) suggesting that ash from a large fire (Fig. 1) may have taken over 6 months before its signal was incorporated into YD-S2. A number of additional peaks in P are evident in Fig. 6, however, these do not show up as peaks in PC3 and are not accompanied by significant peaks in transition metals, for example in 1986 CE where P concentrations increase to > 25 ug g^{-1} (Fig. 6).

Two additional peaks in PC3 are identified in 1974 CE and 1990 CE that are not associated with known fire events in the modern record. A high rainfall event (102 mm) is recorded on January 29, 1990, at Pearce, WA (Bureau of Meteorology station 009053, approximately 33 km SE of Yonderup Cave) and on April 3, 1974 (90 mm) and January 30, 1990 (103 mm) at Gingin, WA (station 009018, approximately 33 km NE of Yonderup Cave). The peaks in PC3 in 1974 and 1990 CE are associated with increases in Zn and Al, and increases in P, Al, and Zn respectively, indicating that intense rainfall could also generate peaks in trace metal concentration in the speleothem. However, there are four occurrences of intense rainfall events (> 90 mm day^{-1}) between 1992 and the removal of the speleothem (Table S9) that did not result in peaks in PC3. Rather, the two peaks in PC3 in the same interval correspond with the 1996 and 2001 fires. This strongly supports our interpretation that peaks in PC3 represent fire events. The identification of fires using PC3 in the paleorecord is also consistent with historical accounts of Indigenous Australian land management which involved frequent low intensity fires to promote plant regrowth and attract game animals for hunting (Hallam, 2014). Historical records indicate that the Noongar people continued this practice until approximately 1830–1860 CE, after which cultural burning was supressed (Abbott, 2002; Hallam, 2014).

The peaks in PC3 are consistent with a dripwater flushing of metal-bearing ash or organic particulate with adsorbed trace-metals derived from the soil. Cerrato et al. (2016) identified an initial post-fire dissolution of metal-carbonate and oxide phases from ash, resulting in a short-term increase in dissolved metals including Al and Fe, however trace metals were also associated with an ash-derived particulate fraction. Plant ash contains a high P content, which can exceed 4% (Sander and Andrén, 1997). Column experiments show that the addition of plant ash to soils results in a 3–10 times increase in extractable P concentrations compared to control soils (Escudey et al., 2010). Notably, P has a high volatilisation temperature (over 774 °C, Bodí et al., 2014), with soil P concentrations shown to increase with increasing fire intensity (Bridges et al., 2019).

5.2. PC1 and PC2 – Aridity and source components

Mg, δ^{13}C and δ^{18}O have previously been interpreted as proxies to distinguish wetter and drier conditions in south-west WA speleothems (Treble et al., 2005) and the inclusion of Br in this group (group A in Fig. 5) is consistent with this (see Supplementary Note 2). We therefore interpret PC1 as a hydroclimate / aridity component, reflecting changes in water–rock interaction (dissolution of host-rock), PCP, salinity (evaporation, dilution) and marine aerosol inputs. Parameters loading positively on PC1 also include elements derived from host-rock dissolution (U, Ba, Sr; group B Fig. 5) in this region (Nagra et al., 2017, Supplementary Note 2) while colloids/OM load negatively on PC1. PC1 reveals that elements derived from host-rock dissolution and marine aerosol inputs both decrease in concentration due to dilution and/or reduced water–rock interaction during periods of high meteoric precipitation. PC2 denotes the separation between aerosol (Br and Mg) components and bedrock-derived elements (Supplementary Note 2), with increases in PC2 associated with greater aerosol inputs.

Overall, PC1 displays multi-decadal behavior with high positive values observed prior to 1900 CE, suggesting drier conditions accompanied by reduced host-rock weathering during 1829–1845 CE and 1868–1887 CE (Fig. 3). PC1 scores become negative after 1900 CE and continue to decline until approximately 1940 CE suggesting reduced water storage times and increased infiltration. After this time and particularly from about 1970 CE onwards, PC1 values begin to increase again up until the time of stalagmite retrieval. This is supported by an increase in PC1 values after 1970 CE which is a known dry period for the region, whereby mean rainfall declined by an average of 12.5% in the wettest months of the year (between May and October) compared to average rainfall during the same months between 1890–2007 (Hope et al., 2010). PC2 shows two periods of strongly negative loadings: 1782–1827 and after 1985 CE (Fig. 5) implying higher host-rock weathering, although the first period is more clearly evident in S only and not Sr and U (Fig. 3) which is consistent with S as a mixed signal at this site (Supplementary Note 2).

5.3. Extended droughts during the 19th century

PC1 has strongly positive values from the 1860s until 1886 CE (Fig. 5) indicating an extended drier period. YD-S2 Mg remains high until 1897 CE before Mg concentrations sharply decrease by 62% (Fig. 3). The δ^{18}O values also remain high until 1897 CE, after which δ^{18}O values drop by 1.7‰. Mg/Ca in dripwater was interpreted as being dominated by prior calcite precipitation (PCP) in southwest Australian caves (Treble et al., 2015; Nagra et al 2016) and consequently, higher speleothem Mg concentrations combined with higher δ^{18}O may indicate enhanced aridity. Mg^{2+} and Sr^{2+} substitute for Ca^{2+} sites in the calcite crystal lattice (Fairchild and Treble, 2009) resulting in a positive relationship between Mg/Ca and Sr/Ca in calcite speleothems where dripwater has been affected by PCP or
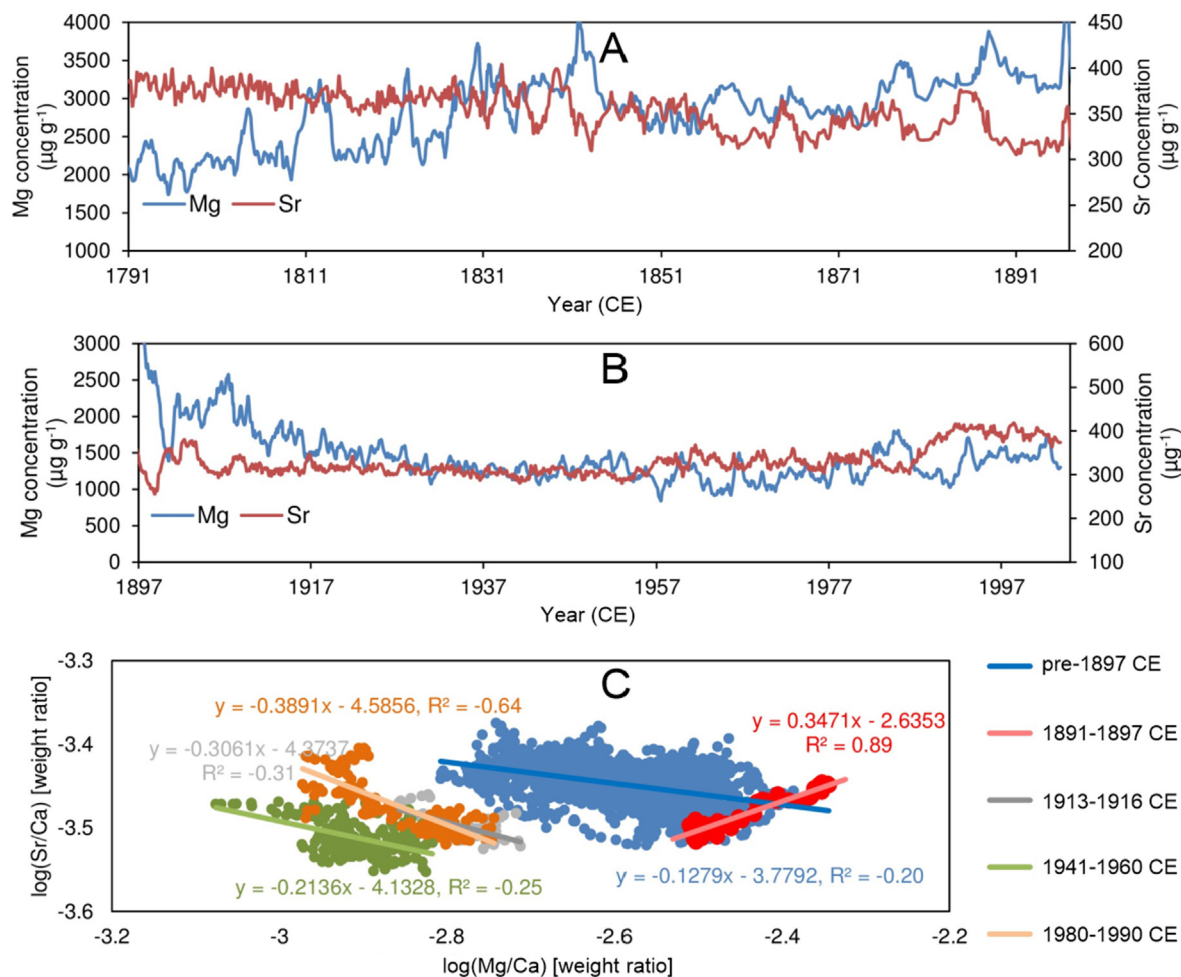
Fig. 7. Plots showing anti-correlation between magnesium (Mg) and strontium (Sr) for pre-fire data (A) and post-fire data (B). C) shows correlations between log natural Sr/Ca and Mg/Ca for all pre-fire data (blue) and a high negative correlation observed for select post-fire periods including 1913 CE – 1916 CE (grey), 1941 CE − 1960 CE (green) and 1980 CE −1990 CE (orange). A strong positive correlation is observed in the 6 years prior to the fire period (red) indicating a limited period where prior calcite precipitation begins to dominate the Sr/Ca and Mg/Ca signals in YD-S2.

water–rock interactions. This was further defined as the slope of the ln(Sr/Ca) vs ln(Mg/Ca) (wt/wt) relationship = 0.88–0.97 by Sinclair et al. (2012). A comparison of the weight ratios of ln(Sr/Ca) and ln(Mg/Ca) shows a negative correlation for most of the time-series, with correlation slopes of between −0.13 and −0.64 (Fig. 7), except for the six year period prior to the 1897 CE event, when a switch to a positive relationship ($R^2 = 0.89$) occurs. It is interpretated here that the negative correlations between Mg/Ca and Sr/Ca ratios that dominate the YD-S2 record are due to the seasonal anti-correlation between Mg/Ca and Sr/Ca ratios; whereby another process appears to dominate the incorporation of Sr in the speleothem on the seasonal scale (see Supplementary Note 2). It seems plausible that during the dry period in the 6 years prior to 1897 CE, the influence of PCP or water–rock interaction (i.e., water–rock interaction) increases sufficiently to override the seasonal signal.

The period of enhanced PCP or water–rock interaction coincides with high $\delta^{18}O$ values (Fig. 3) occurs when PC1 values in the speleothem record indicate an extended dry period since the late 1860s. Reconstructed rainfall from tree rings at a site 370 km ENE from YNP indicates that inland southwest Australia was similarly impacted by a long duration 'megadrought' from 1876 CE to 1908 CE (O'Donnell et al., 2021). The dry period recorded in these tree rings aligns with the timing of the extended dry period in the speleothem record at YNP (1868 ± 14 to 1897 ± 5 CE), particularly given the chronological uncertainty on each of these paleoclimate proxy records. The YD-S2 record confirms that this extended dry period was widespread from the coast to inland WA. The termination of this dry period coincides with the timing of the Australian Federation drought (1891–1903 CE) that affected much of Australia and is captured in the early part of the instrumental climate record (Freund et al., 2017; Godfree et al., 2019) and would

result in ideal conditions under which an extreme fire, marked in our speleothem record at 1897, could occur.

5.4. The inferred 1897 ± 5 CE fire: extreme fire event in YD-S2 record

The short-term peak in $\delta^{18}O$ coinciding with the inferred 1897 CE fire is consistent with the increase in dripwater $\delta^{18}O$ values in Yonderup Cave after the 2005 CE fire (Nagra et al., 2016). This increase was observed for > 5 years after the 2005 CE fire event and was, therefore, attributed to a reduction of canopy cover and albedo causing increased evaporation. In contrast, maximum $\delta^{18}O$ values coincided with the inferred 1897 CE fire, followed by a steep decrease in $\delta^{18}O$ values, which suggests a short period of evaporative concentration caused by heat from the fire (Bian et al., 2019), counteracted by a change in karst hydrology shortly after, as outlined in the following section.

Phosphorus concentrations peak 6.3 times higher than at any other time in the speleothem record in 1897 and are accompanied by high OM (see also the dark banding during 1897 CE in Fig. 4). As discussed in Section 5.1, plant ash contains high P content (Sander and Andrén, 1997) which can result in up to 10 times more P leached compared to control soils (Escudey et al., 2010). Thus the distinct layer of high P and OM in 1897 CE then suggests that a relatively large volume of ash was present above the cave. Delivery of high volumes of impurities is also supported by the micro-hiatus (occlusion of growth sites) and subsequent porosity (where impurities themselves can create pores in the speleothem fabric because they occlude growth sites) recorded in the fabric for approximately 6 years after. The porous fabric is then consistent with inflow of ash-derived particulate and phosphate molecules flushed through fractures and deposited on the surface of the stalagmite, temporarily poisoning growth sites at calcite crystal surfaces (Dove et al., 1993; Lin and Singer, 2005).

The optical continuity in crystal growth before and after the "micro-hiatus" observed in YD-S2, combined with a lack of detectable occurrence of re-nucleation and geometric selection, or detectable dissolution of crystal tips identified on the P map, suggests that the drip rate became very slow or ceased for only a short period of time. Thus, supersaturation or pH remained high enough to ensure optical continuity of the crystallites (cf. Frisia et al., 2000) with the substrate, despite the presence of OM and other impurities that led to a porous fabric. The subsequent abrupt increase in vertical extension rate corroborates the idea of high supersaturation and pH counteracting the effect of impurities on calcite precipitation following the inferred 1897 CE fire (Fig. 3). Nagra et al. (2016) report that 30% of the area above Yonderup Cave is exposed bedrock, therefore direct exposure of limestone to high temperatures during an extreme fire event may cause localised lime formation in the soil or upper epikarst. Subsequent dissolution could have resulted in an increase in alkalinity and supersaturation in dripwater, enhancing speleothem extension rates (Fig. 3).

Reduced S concentration is also observed at the timing of the event (Fig. 4) suggesting some S is sourced from the vegetation and was likely volatilised during the fire due to its low volatilisation temperature (375 °C – 575 °C, Bodí et al., 2014). In some locations where dripwater S may be predominantly derived from vegetation, S may become source-limited for a prolonged period post-fire due to the removal of overlying vegetation (Treble et al., 2016), with the duration of vegetation loss post-fire depending on the season of the burn. For example, Hobbs and Atkins (1990) reported more rapid vegetative regrowth in Banksia woodland after spring fires compared to autumn fires. The opposite loading of S compared to aerosol-sourced Mg and Br on PC2 suggests that the predominant source of S within YD-S2 may be derived from the bedrock, however this is unlikely given that published studies from four different caves document that bedrock S contribution to dripwaters is minor (between 1.1% – 2.1%, Wynn et al., 2008; Wynn et al., 2010; Wynn et al., 2013). Rather, the positive relationship between S and bedrock sourced parameters such as Sr and Ba, may result from a pH control on S incorporation into speleothems (Wynn et al., 2014; Wynn et al., 2018). This may be the cause for the drop in S concentration observed in 1897 CE, whereby an increase in dripwater pH caused by calcination of the limestone above the cave could result in a decline in S due to relatively higher carbonate than sulphate incorporation.

Using the geochemical proxies considered here, we interpret that the period from 1760 CE until approximately 1825 CE was characterised by low intensity, high frequency fire events in the region. There are two drier periods observed in the YD-S2 record between approximately 1827–1840 CE and 1859–1886 CE. The dry period observed between the late 1820s to 1840 CE is supported by historical handwritten weather records where a period of very low rainfall in the Perth region was recorded between the 1830s–1840s (Gergis et al., 2021). The conclusion of the dry period between approximately 1960s to 1890 is evident in the instrumental record known as the Federation Drought and the tree ring record (O'Donnell et al 2021). The YD-S2 record shows that this extended dry period resulted in an enhanced PCP and/or host rock weathering signal and culminated in a significant fire in 1897 ± 5 CE. PC3 maxima coinciding with maxima in $\delta^{18}O$ and Mg as well as post-fire shifts in OM and metal concentrations highlight that the inferred 1897 ± 5 CE fire was an unusually extreme event in the last two centuries of YD-S2′s growth history that affected the karst water balance, speleothem crystal fabric, extension rate and pulse-concentration of metals associated with ash and/or soil. The intensity of the fire was likely exacerbated by multi-decadal drought, but possibly also due to a transition away from cultural burning practices by Indigenous Australians which may have resulted in build-up of understorey vegetation and dry combustible material on the forest floor.

5.5. Changes in surface-cave hydrology and climate after the inferred 1897 ± 5 CE fire

The prolonged decline in $\delta^{18}O$ values after the inferred 1897 CE wildfire event suggests an increase in rainfall infiltration, likely coinciding with a reduction in evaporation

and evapotranspiration due to decreased water storage and vegetation cover. We interpret this trend as an effect of the heating of the limestone and soil, which resulted in increased meso- and macro-porosity of the whole epikarst. This then likely yielded a faster transmission of rainfall into the aquifer, reduced water storage times, and is consistent with the increased colloid/OM incorporation observed in YD-S2 (Fig. 3). Fracturing of the limestone above Yonderup Cave has been observed after a fire which occurred in 2005 CE just prior to the removal of YD-S2 and has been documented in Nagra et al. (2016). OM particulate in speleothems has been commonly ascribed as originating in the soil/surface zone (Hartland et al., 2012) and can be adsorbed at calcite crystal surfaces, thus marking their tips during speleothem growth as determined by both optical and fluorescent layers (Baker et al., 2008). When OM is dissolved in the water, it is most likely incorporated within the speleothem to yield pervasive fluorescence (Ramseyer et al., 1997). The observation of increased adsorption of OM particulate onto the speleothem post-fire may be the result of reduced physical filtering of OM colloids due to increased porosity and ash-related abundance of OM compounds.

The decline in PC1 observed after the inferred 1897 CE fire event indicates an overall dilution effect enhanced by the increase in epikarst porosity post-fire. YD-S2 $\delta^{18}O$ values show an initial increase at 1897 CE, suggesting that they are initially affected by the impact of evaporation on water balance during the intense heat of the fire, but subsequently decrease post-fire due to the increase in soil/host rock porosity, reduced water–rock interaction and/or increases dilution. Elements such as Br, Sr, Ba and U slowly decline between approximately 1900–1960 CE. This period has been identified from instrumental data as being relatively wetter in south-west WA as identified by changepoints in rainfall timeseries data for the region (Hope et al., 2010). This is supported by lower $\delta^{18}O$ values throughout this period, which indicate that larger rainfall events impact in the region at this time. The lower $\delta^{18}O$ values may also be enhanced by post-fire increased bedrock permeability or fracture flow. The decline in PC1 in the early to mid-1900s CE, therefore, appears to reflect a mixed signal of dilution, resulting from increased rainfall, and decreased water–rock interaction resulting from a shift in epikarst hydrology following extreme fire. The reconstructed changes in hydrology post-1897 CE fire event at Yonderup cave and its impacts on dripwater chemistry and speleothem growth are summarised in Fig. 8.

5.6. Speleothem trace metals as proxies for fire intensity

The speleothem evidence is for an extreme fire in 1897 with high P and Zn. We note that the height of the PC3 peak may not be representative of the fire intensity. For example, moderate intensity events could result in particularly high PC3 peaks, i.e., increase loadings of multiple metals on PC3, if the burn temperature is hot enough to
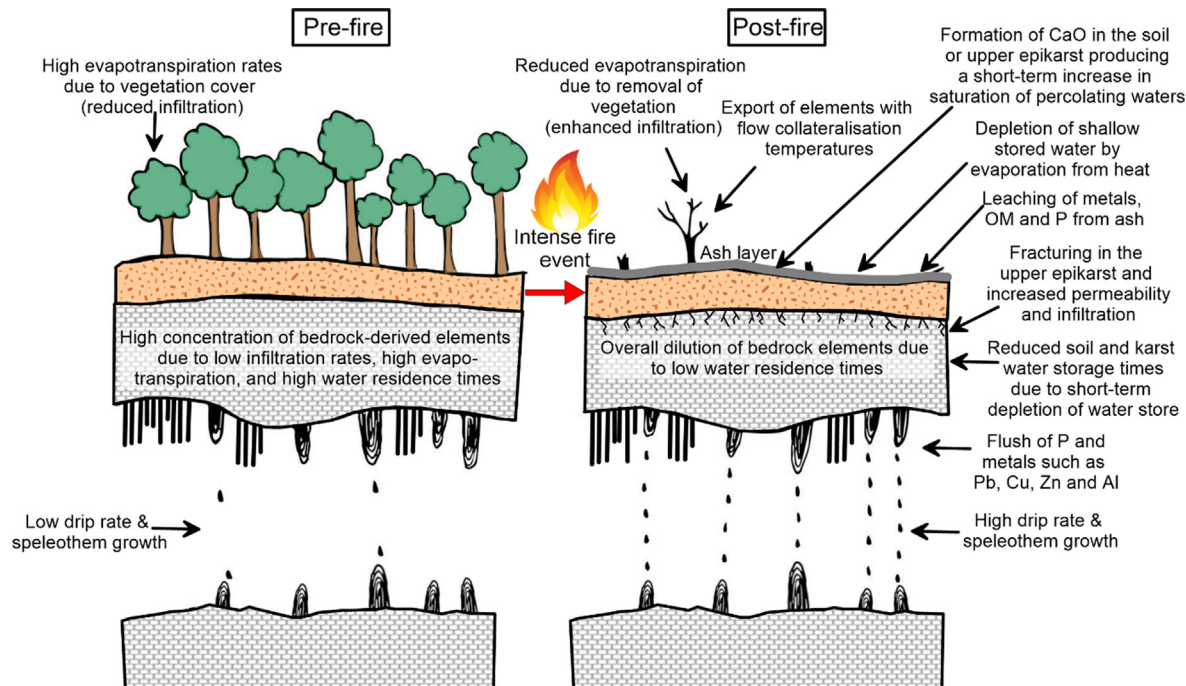

Fig. 8. Conceptual figure showing the impacts of extreme fire on stalagmite YD-S2. The reduction in post-fire vegetation cover results in reduced evapotranspiration and subsequent increased infiltration of precipitation into the bedrock which is further enhanced by fracturing of the upper epikarst. Overall, bedrock and aerosol-derived parameters are reduced due to dilution and reduced water residence times resulting from enhanced meso- and macro-porosity. The combustion of vegetation results in an ash layer containing OM, P and metals which are leached into the subsurface and incorporated into the speleothem.

generate ash but too cool to result in volatilisation of elements. Alternatively, volatilisation of elements during extremely high intensity events, and less ash created during low intensity events could both potentially result in lower PC3 peaks, suggesting that this geochemical technique may be most useful for identification of moderate intensity or large-scale fire events. Christensen and Abbott (1989) determined that low intensity fires do not dramatically affect soil properties and nutrient cycling in eucalypt forest ecosystems in SW WA. However, it is noted that the spatial distribution of different trace metals in ash varies depending on the vegetation species within that local catchment and the microtopography of the soil (Pereira and Úbeda, 2010), likely resulting in differences in trace metal composition of dripwater after wildfires.

Finally, hydrology likely has an impact on the concentration and incorporation of trace metals into dripwater, which may make the fire signal recorded in the speleothem inconsistent between events. For example, immediate rainfall after application of nutrients to soils results in higher nutrient leaching compared to when there is a delay between nutrient application and rainfall as this prevent solutes from diffusing into intra- and inter-aggregate pore spaces (McLay et al., 1991). A single large recharge event immediately following a fire may flush the ash through the system and result in a large peak in metals and P, versus an attenuated peak from less intense rainfall. The relationship between metals and fire intensity requires further investigation using modern speleothems that grew during known fire events, particularly more recent fire events for which fire intensity can be derived using satellite data (cf. Treble et al., 2016). This is the subject of future research.

6. CONCLUSIONS

This study utilises a large suite of analyses including stable isotopes (δ^{13}C, δ^{18}O), elemental and organic matter concentrations, as well as a thorough understanding of the karst hydrology and fire response determined from previous cave monitoring, to establish a combined fire and climate record for a Western Australian cave site. We provide a novel demonstration of the ability to pinpoint the timing of paleo-fire events, particularly when they form in shallow cave settings. The results from this study reveal that in Yonderup Cave, particularly intense wildfires may translate into speleothems as increases in soil and ash-derived elements such as P, Al and Cu coupled with maxima in δ^{13}C and Mg, and short-term increases in δ^{18}O after evaporative enrichment. In contrast, lower intensity fires may appear as pulses in different combinations of metals (Cu, Pb, Al, Zn) and P, and may not be associated with obvious increases in bedrock-derived elements such as Sr, Ba, and U. Traditional suites of bedrock-derived elements (Mg, Sr, Ba) therefore, do not appear to be reliable indicators of fire. Rather, these elements are useful for interpreting climate leading up to a fire event, as well as PCP and changes in hydrology post-fire.

Decreases in δ^{18}O, Ba, U, Sr, Br and Mg concentrations after the inferred 1897 CE fire event indicate a transition from dry to wet conditions. However, we also present evidence for a significant change in karst hydrology caused by extreme heat from the inferred 1897 fire event that likely resulted in a non-linear response in these proxies to the environmental impact of the fire. The decline in water–rock interaction resulting from changes in the post-fire bedrock hydrology demonstrates how hydroclimate proxies in fire prone regions could be exaggerated and hence misinterpreted without taking into account the impact of fires. Fire events may result in an increase in OM flushed through fractures or widened pores, which could also be misinterpreted as higher amounts of surface vegetation. These findings are particularly relevant for paleoclimate studies of shallow caves in water-limited environments with thin soil profiles where the impact of fire events should be taken into account.

The Br record for YD-S2 demonstrates its applicability for use as a water balance proxy in speleothems and suggests that it may be particularly useful at sites within close proximity to the coastline, due to its marine aerosol source, although care should be exercised in interpreting water balance from Br or other hydroclimate sensitive proxies in shallow caves in fire-prone regions where the heat from fires could produce a non-linear response. This study also confirms the importance of using high quality, non-porous samples when using this technique to identify paleo-fire events in speleothems, and 2D depictions of speleothem laminae for chronologies where available.

Finally, this record has extended knowledge on potential climate conditions leading to fire for a region with both sparse paleoclimate information and sparse paleofire information. The existence of two multi-decadal droughts corroborates a dendrochronological record and an historical reconstruction that droughts impacted the wider Perth region, an area of increasing water stress due to climate change and water extraction. This study also highlights differences in the frequency and possible intensity of fires in the pre- versus post-European colonisation management of the land, with the evidence here supporting more frequent, low intensity burning during Indigenous management contrasting with less frequent more intense fires after colonisation. This transition is also marked in the speleothem record by an extreme fire event exacerbated by multi-decadal drought and possibly also by fuel build-up consistent with the change in land management practices.

Declaration of Competing Interest

ACKNOWLEDGEMENT

AUTHOR CONTRIBUTIONS

FUNDING

APPENDIX A. SUPPLEMENTARY DATA

Supplementary data to this article can be found online at https://doi.org/10.1016/j.gca.2022.03.020.

REFERENCES

Abbott I. (2002) *Historical records of Noongar fires, 1658–1888: a compendium.* Dept. of Conservation & Land Management, Kensington, W.A..

Baker A., Mariethoz G., Comas-Bru L., Hartmann A., Frisia S., Borsato A., Treble T. and Asrat A. (2021) The properties of annually laminated stalagmites – A global synthesis. *Rev. Geophys.* **59**, e2020RG000722.

Baker A., Smith C. L., Jex C., Fairchild I. J., Genty D. and Fuller L. (2008) Annualy laminated speleothems: a review. *Int. J. Speleology* **37**, 193–206.

Baldini J. U. L., McDermott F., Hoffman D. L., Richards D. A. and Clipson N. (2008) Very high-frequency and seasonal cave atmosphere P_{CO2} variability: Implications for stalagmite growth and oxygen isotope-based paleoclimate records. *Earth Planet. Sci. Lett.* **272**, 118–129.

Ban F., Baker A., Marjo C. E., Duan W., Li X., Han J., Coleborn K., Akter R., Tan M. and Nagra G. (2018) An optimized chronology for a stalagmite using seasonal trace element cycles from Shihua Cave, Beijing, North China. *Sci. Rep.* **8**, 1–9.

Bar-Matthews M., Ayalon A. and Kaufman A. (1997) Late Quaternary paleoclimate in the Eastern Mediterranean region from stable isotope analysis of speleothems at Soreq Cave, Israel. *Quat. Res.* **47**, 155–168.

Beard J. S., Beeston G. R., Harvey J., Hopkins A. J. M. and Shepherd D. P. (2013) The vegetation of Western Australia at the 1:3,000,000 scale. Explanatory memoir. *Second edition. Conservation Science Western Australia* **9**, 1–152.

Beck H., Zimmermann N., McVicar T., Vergopolan N., Berg A. and Wood E. F. (2018) Present and future Köppen-Geiger climate classification maps at 1-km resolution. *Sci. Data* **5** 180214.

Bian F., Coleborn K., Flemons I., Baker A., Treble P. C., Hughes C. E., Baker A., Andersen M. S., Tozer M. G., Duan W., Fogwill C. J. and Fairchild I. J. (2019) Hydrological and geochemical responses of fire in a shallow cave system. *Sci. Total Environ.* **662**, 180–191.

Bodí M. B., Martin D. A., Balfour V. N., Santín C., Doerr S. H., Pereira P., Cerdà A. and Mataix-Solera J. (2014) Wildland fire ash: Production, composition and eco-hydro-geomorphic effects. *Earth Sci. Rev.* **130**, 103–127.

Borsato A., Frisia S., Fairchild I. J., Somogyi A. and Susini J. (2007) Trace element distribution in annual stalagmite laminae mapped by micrometer-resolution X-ray fluorescence: implications for incorporation of environmentally significant species. *Geochim. Cosmochim. Acta* **71**, 1494–1512.

Borsato A., Frisia F., Howard D. and Greig A. (2021) A guide to synchrotron hard X-ray fluorescence mapping of annually laminated stalagmites: sample preparation, analysis and evaluation. *Spectrochim. Acta, Part B*.

Bridges J. M., Petropoulos G. P. and Clerici N. (2019) Immediate changes in organic matter and plant available nutrients of Haplic Luvisol soils following different experimental burning intensities in Damak Forest, Hugary. *Forests* **10**, 27–36.

Bryan E., Meredith K. T., Baker A., Andersen M. S. and Post V. E. A. (2017) Carbon dynamics in a Late Quaternary-age coastal limestone aquifer system undergoing saltwater intrusion. *Sci. Total Environ.* **607–608**, 771–785.

Butler O. M., Elser J. J., Lewis T., Mackey B. and Chen C. (2018) The phosphorus-rich signature of fire in the soil–plant system: a global meta-analysis. *Ecol. Lett.* **21**, 335–344.

Cerrato J. M., Blake J. M., Hirani C., Clark A. L., Ali A. M., Artyushkova K., Peterson E. and Bixby R. J. (2016) Wildfires and water chemistry: effect of metals associated with wood ash. *Environ. Sci.: Processes & Impacts* **8**, 1078–1089.

Certini G. (2005) Effects of fire on properties of forest soils: a review. *Oecologia* **143**, 1–10.

Cheng H., Spötl C., Breitenbach S. F. M., Sinha A., Wassenburg J. A., Jochum K. P., Scholz D., Li X., Yi L., Peng Y., Lv Y., Zhang P., Votintseva A., Loginov V., Ning Y., Kathayat G. and Edwards R. L. (2016) Climate variations of Central Asia on orbital to millennial timescales. *Sci. Rep.* **6**, 36975.

Christensen P. and Abbott I. (1989) Impact of fire in the eucalypt forest ecosystem of southern Western Australia: a critical review. *Australian Forestry* **52**, 103–121.

Clark T. R., Zhao J.-X., Roff G., Feng Y.-X., Done T. J., Nothdurft L. D. and Pandolfi J. M. (2014) Discerning the timing and cause of historical mortality events in modern Porites from the Great Barrier Reef. *Geochim. Cosmochim. Acta* **138**, 57–80.

Coleborn K., Spate A., Tozer M., Andersen M. S., Fairchild I. J., MacKenzie B., Treble P. C., Meehan S., Baker A. and Baker A. (2016) Effects of wildfire on long-term soil CO_2 concentration: implications for karst processes. *Environ. Earth Sci.* **75**, 330.

DeBano L. F. (2000) The role of fire and soil heating on water repellency in wildland environments: a review. *J. Hydrol.* **231–232**, 195–206.

[dataset] Department of Biodiversity, Conservation and Attractions (2020) "DBCA Fire History (DBCA-060)". Available at: https://catalogue.data.wa.gov.au/dataset/dbca-fire-history. Retrieved November 27, 2020.

Department of Conservation and Land Management (1989). *Yanchep National Park Management Plan 1989-1999*. Como, Western Australia.

Department of Environment and Conservation (2010) Parks and Reserves of Yanchep and Neerabup Draft Management Plan 2010. Available at https://library.dbca.wa.gov.au/static/Full-TextFiles/025376.pdf. Retrieved January 15, 2021.

Dlapa P., Simkovic I., Doerr S. H., Simkovic I., Kanka R. and Mataix-Solera J. (2008) Application of thermal analysis to elucidate water-repellency changes in heated soils. *Soil Sci. Soc. Am. J.* **72**, 1–10.

Dorale J. A., Edwards R. L., Ito E. and Gonzalez L. A. (1998) Climate and vegetation history of the midcontinent from 75 to 25 ka: a speleothem record from Crevice Cave, Missouri, USA. *Science* **282**, 1871–1874.

Dove P. M. and Hochella, Jr, M. F. (1993) Calcite precipitation mechanisms and inhibition by orthophosphate: In situ observations by Scanning Force Microscopy. *Geochim. Cosmochim. Acta* **57**, 705–714.

Escudey M., de la Fuente P., Antilén M. and Molina M. (2010) Effect of ash from forest fires on phosphorus availability, transport, chemical forms, and content in volcanic soils. *Environ. Chem.* **7**, 103–110.

Fairchild I. J. and Treble P. C. (2009) Trace elements in speleothems as recorders of environmental change. *Quat. Sci. Rev.* **28**, 449–468.

Faraji M., Borsato A., Frisia S., Hellstrom J., Lorrey A., Hartland A., Greig A. and Mattey D. P. (2021) Accurate dating of stalagmites from low seasonal contrast tropical Pacific climate using Sr 2D maps, fabrics and annual hydrological cycles. *Sci. Rep.* **11**.

Freund M., Henley B. J., Karoly D. J., Allen K. J. and Baker P. J. (2017) Multi-century cool- and warm-season rainfall reconstructions for Australia's major climatic regions. *Clim. Past* **13**, 1751–1770.

Frisia S. (2015) Microstratigraphic logging of calcite fabrics in speleothems as tool for palaeoclimate studies. *Int. J. Speleology* **44**, 1–16.

Frisia S. and Borsato A. (2010) Karst. In *Developments in Sedimentology* (eds. A. M. Alonso-Zarza and L. H. Tanner). Elsevier, pp. 269–318.

Frisia S., Borsato A., Fairchild I. and McDermott F. P. (2000) Calcite fabrics, growth mechanisms, and environments of formation in speleothems from the Italian Alps and South-western Ireland. *J. Sediment. Res.* **70**, 1183–1196.

Gagan M. K., Chivas A. R. and Isdale P. J. (1994) High-resolution isotopic records from corals using ocean temperature and mass-spawning chronometers. *Earth Planet. Sci. Lett.* **121**, 549–558.

Genty D. and Quinif Y. (1996) Annually laminated sequences in the internal structure of some Belgian stalagmites; importance for paleoclimatology. *J. Sediment. Res.* **66**, 275–288.

Gergis J., Baillie Z., Ingallina S., Ashcroft L. and Ellwood T. (2021) A historical climate dataset for southwestern Australia, 1830–1875. *Int. J. Climatol.* **1–22**.

Godfree R. C., Knerr N., Godfree D., Busby J., Robertson B. and Encinas-Viso F. (2019) Historical reconstruction unveils the risk of mass mortality and ecosystem collapse during pancontinental megadrought. *Proc. Natl. Acad. Sci.* **116**, 15580.

Grove T. S., O'Connell A. M. and Dimmock G. M. (1986) Nutrient changes in surface soils after an intense fire in jarrah (*Eucalyptus marginata* Donn ex Sm.) forest. *Aust. J. Ecol.* **11**, 303–317.

Hallam S. J. (2014) *Fire and Hearth a study of Aboriginal usage and European usurpation in south-western Australia*, Revised Edition. UWA Publishing, Crawley, Western Australia.

Harper A. R., Santin C., Doerr S. H., Froyd C. A., Albini D., Otero X. L., Viñas L. and Pérez-Fernández B. (2019) Chemical composition of wildfire ash produced in contrasting ecosystems and its toxicity to *Daphnia magna*. *Int. J. Wildland Fire* **28**, 726–737.

Hartland A., Fairchild I., Lead J., Dominguez-Villar D., Baker A., Gunn J., Baalousha M., Ju-Nam Y. and Ju-Nam Y. K. (2010) The dripwaters and speleothems of Poole's Cavern: a review of recent and ongoing research. *Cave and Karst Science* **36**, 37–46.

Hartland A., Fairchild I. J., Lead J. R., Zhang H. and Baalousha M. (2011) Size, speciation and lability of NOM–metal complexes in hyperalkaline cave dripwater. *Geochim. Cosmochim. Acta* **75**, 7533–7551.

Hartland A., Fairchild I. J., Lead J. R., Borsato A., Baker A., Frisia S. and Baalousha M. (2012) From soil to cave: transport of trace metals by natural organic matter in karst dripwaters. *Chem. Geol.* **304–305**, 68–82.

Hellstrom J., McCulloch M. and Stone J. (1998) A Detailed 31,000-Year Record of Climate and Vegetation Change, from the Isotope Geochemistry of Two New Zealand Speleothems. *Quat. Res.* **50**, 167–178.

Heydari M., Rostamy A., Najafi F. and Dey D. C. (2017) Effect of fire severity on physical and biochemical soil properties in Zagros oak (Quercus brantii Lindl.) forests in Iran. *J. For. Res.* **28**, 95–104.

Hobbs R. J. and Atkins L. (1990) Fire-related dynamics of a *Banksia* woodland in south-western Western Australia. *Aust. J. Bot.* **38**, 97–110.

Hogue B. A. and Inglett P. W. (2012) Nutrient release from combustion residues of two contrasting herbaceous vegetation types. *Sci. Total Environ.* **431**, 9–19.

Hope P., Timbal B. and Fawcett R. (2010) Associations between rainfall variability in the southwest and southeast of Australia and their evolution through time. *Int. J. Climatol.* **30**, 1360–1371.

Hopley P. J., Marshall J. D., Weedon G. P., Latham A. G., Herries A. I. and Kuykendall K. L. (2007) Orbital forcing and the

spread of C4 grasses in the late Neogene: stable isotope evidence from South African speleothems. *J. Hum. Evol.* **53**, 620–634.

Kassambara, A. and Mundt, F. (2020) Factoextra: extract and visualise the results of multivariate data analyses. R package v1.0.7. https://CRAN.R-project.org/package=factoextra.

Kemperl J. and Maček J. (2009) Precipitation of calcium carbonate from hydrated lime of variable reactivity, granulation and optical properties. *Int. J. Miner. Process.* **93**, 84–88.

Killick R., Fearnhead P. and Eckley I. A. (2012) Optimal detection of changepoints with a linear computational cost. *J. Am. Stat. Assoc.* **107**, 1590–1598.

Lansangan J. R. G. and Barrios E. B. (2009) Principal components analysis of nonstationary time series data. *Statistics and Computing* **19**, 173–187.

Lê S., Josse J. and Husson F. (2008) FactoMineR: an R package for multivariate analysis. *J. Stat. Softw.* **25**, 18.

Lin Y. P. and Singer P. C. (2005) Inhibition of calcite crystal growth by polyphosphates. *Water Res.* **39**, 4835–4843.

Lipar M. and Webb J. A. (2014) Middle–late Pleistocene and Holocene chronostratigraphy and climate history of the Tamala Limestone, Cooloongup and Safety Bay Sands, Nambung National Park, southwestern Western Australia. *Aust. J. Earth Sci.* **61**, 1023–1039.

Marcus M. A., MacDowell A. A., Celestre R., Manceau A., Miller T., Padmore H. A. and Sublett R. E. (2004) Beamline 10.3.2 at ALS: a hard X-ray microprobe for environmental and materials sciences. *J. Synchrotron Radiation* **11**, 239–147.

Mast M. A. and Clow D. W. (2008) Effects of 2003 wildfires on stream chemistry in Glacier National Park, Montana. *Hydrol. Process.* **22**, 5013–5023.

McCaw W. L. and Hanstrum B. (2003) Fire environment of Mediterranean south-west Western Australia. In *Fire in ecosystems of south-west Western Australia: impacts and management* (eds. I. Abbott and N. Burrows). Backhuys Publishers, Leiden, The Netherlands, pp. 87–106.

McLay C. D. A., Cameron K. C. and McLaren R. G. (1991) Effect of time of application and continuity of rainfall on leaching of surface-applied nutrients. *Soil Phys. Hydrology* **29**, 1–9.

Meng Q.-B., Wang C.-K., Liu J.-F., Zhang M.-W., Lu M.-M. and Wu Y. (2020) Physical and micro-structural characteristics of limestone after high temperature exposure. *Bull. Eng. Geol. Environ.* **79**, 1259–1274.

Moreira F., Ascoli D., Safford H., Adams M. A., Moreno J. M., Pereira J. M. C., Catry F. X., Armesto J., Bond W., González M. E., Curt T., Koutsias N., McCaw L., Price O., Pausas J. G., Rigolot E., Stephens S., Tavsanoglu C., Vallejo V. R., Van Wilgen B. W., Xanthopoulos G. and Fernandes P. M. (2020) Wildfire management in Mediterranean-type regions: paradigm change needed. *Environ. Res. Lett.* **15** 011001.

Moropoulou A., Bakolas A. and Aggelakopoulou E. (2001) The effects of limestone characteristics and calcination temperature to the reactivity of the quicklime. *Cem. Concr. Res.* **31**, 633–639.

Nagra G., Treble P. C., Andersen M. S., Bajo P., Hellstrom J. and Baker A. (2017) Dating stalagmites in mediterranean climates using annual trace element cycles. *Sci. Rep.* **7**.

Nagra G., Treble P. C., Andersen M. S., Fairchild I. J., Coleborn K. and Baker A. (2016) A post-wildfire response in cave dripwater chemistry. *Hydrol. Earth Syst. Sci.* **20**, 2745–2758.

O'Donnell A. J., McCaw W. L., Cook E. R. and Grierson P. F. (2021) Megadroughts and puvials in southwest Australia: 1350–2017 CE. *Clim. Dyn.*.

Orland I. J., Burstyn Y., Bar-Matthews M., Kozdon R., Ayalon A., Matthews A. and Valley J. W. (2014) Seasonal climate signals (1990–2008) in a modern Soreq Cave stalagmite as revealed by high-resolution geochemical analysis. *Chem. Geol.* **363**, 322–333.

Pereira P. and Úbeda X. (2010) Spatial distribution of heavy metals released from ashes after a wildfire. *J. Environ. Eng. Landscape Manage.* **18**, 13–22.

Petticrew E. L., Owens P. N. and Giles T. R. (2006) Wildfire Effects on the Quantity and Composition of Suspended and Gravel-Stored Sediments. In *The Interactions Between Sediments and Water* (eds. B. Kronvang, J. Faganeli and N. Ogrinc). Springer, Netherlands, Dordrecht, pp. 283–292.

Playford, P.E., Cockbain, A.E. and Low, G.H. (1976) Geology of the Perth Basin Western Australia. Geological Survey of Western Australia, Bulletin 124.

Playford, P.E., Cockbain, A.E., Berry, P.F., Roberts, A.P., Haines, P.W., and Brooke, B.P. (2013) Geology of Shark Bay. Geological Survey of Western Australia, Bulletin 146.

Plumlee, G.S., Martin, D.A., Hoefen, T., Kokaly, R., Hageman, P., Eckberg, A., Meeker, G.P., Adams, M., Anthony, M. and Lamothe, P.J. (2007) Preliminary Analytical Results for Ash and Burned Soils from the October 2007 Southern California Wildfires: U.S. Geological Survey Open-File Report 2007–1407. U.S. Geological Survey, Reston, Virginia.

Quigley K. M., Kolka R., Sturtevant B. R., Dickinson M. B., Kern C. C. and Miesel J. R. (2021) Restoring open canopy pine barrens from the ground up: Repeated burns correspond with increased soil hydraulic conductivity. *Sci. Total Environ.* **767** 144258.

Quigley K. M., Wildt R. E., Sturtevant B. R., Kolka R. K., Dickinson M. B., Kern C. C., Donner D. M. and Miesel J. R. (2019) Fuels, vegetation, and prescribed fire dynamics influence ash production and characteristics in a diverse landscape under active pine barrens restoration. *Fire Ecol.* **15**.

Ramseyer K., Miano T. M., D'Orazio V., Wildberger A., Wagner T. and Geister J. (1997) Nature and origin of organic matter in carbonates from speleothems, marine cements and coral skeletons. *Org Geochem.* **26**, 361–378.

Revchuk A. D. and Suffet I. H. (2014) Effect of Wildfires on Physicochemical Changes of Watershed Dissolved Organic Matter. *Water Environ. Res.* **86**, 372–381.

Rouquerol J., Avnir D., Fairbridge C. W., Everett D. H., Haynes J. M., Pernicone N., Ramsay J. D. F., Sing K. S. W. and Unger K. K. (1994) Recommendations for the characterization of porous solids (Technical Report). *Pure Appl. Chem.* **66**, 1739–1758.

Ryan C. G., Etschmann B. E., Vogt S., Maser J., Harland C. L., van Achterbergh E. and Legnini D. (2005) Nuclear microprobe – synchrotron synergy: Towards integrated quantitative real-time elemental imaging using PIXE and SXRF. *Nucl. Instrum. Methods Phys. Res., Sect. B* **231**, 183–188.

Ryan C. G., Jamieson D. N., Churms C. L. and Pilcher J. V. (1995) A new method for on-line true-elemental imaging using PIXE and the proton microprobe. *Nucl. Instrum. Methods Phys. Res., Sect. B* **104**, 157–165.

Ryan S. E., Dwire K. A. and Dixon M. K. (2011) Impacts of wildfire on runoff and sediment loads at Little Granite Creek, western Wyoming. *Geomorphology* **129**, 113–130.

Sander M. L. and Andrén O. (1997) Ash from Cereal and Rape Straw Used for Heat Production: Liming Effect and Contents of Plant Nutrients and Heavy Metals. *Water Air Soil Pollut.* **93**, 93–108.

Savage S. M. (1974) Mechanism of Fire-Induced Water Repellency in Soil. *Soil Sci. Soc. Am. J.* **38**, 652–657.

Savitzky A. and Golay M. J. E. (1964) Smoothing and differentiation of data by simplified least squares procedures. *Anal. Chem.* **36**, 1627–1639.

Schaller J., Tischer A., Struyf E., Bremer M., Belmonte D. U. and Potthast K. (2015) Fire enhances phosphorus availability in topsoils depending on binding properties. *Ecology* **96**, 1598–1606.

Scott A. J. and Knott M. (1974) A cluster analysis method for grouping means in the analysis of variance. *Biometrics* **30**, 507–512.

Sinclair D. J., Banner J. L., Taylor F. W., Partin J., Jenson J., Mylroie J., Goddard E., Quinn T., Jocson J. and Miklavič B. (2012) Magnesium and strontium systematics in tropical speleothems from the Western Pacific. *Chem. Geol.* **294–295**, 1–17.

Smith A. J., Massuel S. and Pollock D. W. (2012) Geohydrology of the Tamala Limestone Formation in the Perth Region: Origin and role of secondary porosity. *CSIRO*, 63.

Spencer C. N., Gabel K. O. and Hauer F. R. (2003) Wildfire effects on stream food webs and nutrient dynamics in Glacier National Park, USA. *For. Ecol. Manage.* **178**, 141–153.

Stoof C. R., Slingerland E. C., Mol W., van den Berg J., Vermeulen P. J., Ferreira A. J. D., Ritsema C. J., Parlange J.-Y. and Steenhuis T. S. (2014) Preferential flow as a potential mechanism for fire-induced increase in streamflow. *Water Resour. Res.* **50**, 1840–1845.

Treble P. C., Chappell J., Gagan M. K., McKeegan K. D. and Harrison T. M. (2005) In situ measurement of seasonal δ^{18}O variations and analysis of isotopic trends in a modern speleothem from southwest Australia. *Earth Planet. Sci. Lett.* **233**, 17–32.

Treble P., Shelley J. M. G. and Chappell J. (2003) Comparison of high resolution sub-annual records of trace elements in a modern (1911–1992) speleothem with instrumental climate data from southwest Australia. *Earth Planet. Sci. Lett.* **216**, 141–153.

Treble P. C., Fairchild I. J., Baker A., Meredith K. T., Andersen M. S., Salmon S. U., Bradley C., Wynn P. M., Hankin S. I., Wood A. and McGuire E. (2016) Roles of forest bioproductivity, transpiration and fire in a nine-year record of cave dripwater chemistry from southwest Australia. *Geochim. Cosmochim. Acta* **184**, 132–150.

Treble P. C., Fairchild I. J., Griffiths A., Baker A., Meredith K. T., Wood A. and McGuire E. (2015) Impacts of cave air ventilation and in-cave prior calcite precipitation on Golgotha Cave dripwater chemistry, southwest Australia. *Quat. Sci. Rev.* **127**, 61–72.

Valverde J. M., Sanchez-Jimenez P. E. and Pérez-Maqueda L. A. (2015) Limestone calcination nearby equilibrium: kinetics, CaO crystal structure, sintering and reactivity. *J. Phys. Chem. C* **119**, 1623–1641.

Wang L., Xue Z., Cai J. and Hu B. (2019) Relationship Between Microstructure and Properties of Limestone Calcined Rapidly at High Temperatures. *Trans. Indian Inst. Met.* **72**, 3215–3222.

Wang Y., Cheng H., Edwards R. L., Kong X., Shao X., Chen S., Wu J., Jiang X., Wang X. and An Z. (2008) Millennial- and orbital-scale changes in the East Asian monsoon over the past 224,000 years. *Nature* **451**, 1090–1093.

Weber M., Scholz D., Schröder-Ritzrau A., Deininger M., Spötl C., Lugli F., Mertz-Kraus R., Jochum K. P., Fohlmeister J., Stumpf C. F. and Riechelmann D. F. C. (2018) Evidence of warm and humid interstadials in central Europe during early MIS 3 revealed by a multi-proxy speleothem record. *Quat. Sci. Rev.* **200**, 276–286.

Wotton B. M., Gould J. S., McCaw W. L., Cheney N. P. and Taylor S. W. (2012) Flame temperature and residence time of fires in dry eucalypt forest. *Int. J. Wildland Fire* **21**, 270–281.

Wu G. and Wang D. Y. (2012) Mechanical and acoustic emission characteristics of limestone after high temperature. *Adv. Mater. Res.* **446–449**, 23–28.

Wynn P. M., Fairchild I. J., Baker A., Baldini J. U. L. and McDermott F. (2008) Isotopic archives of sulphate in speleothems. *Geochim. Cosmochim. Acta* **72**, 2465–2477.

Wynn P. M., Fairchild I. J., Frisia S., Spötl C., Baker A. and Borsato A. (2010) High-resolution sulphur isotope analysis of speleothem carbonate by secondary ionisation mass spectrometry. *Chem. Geol.* **271**, 101–107.

Wynn P. M., Borsato A., Baker A., Frisia S., Miorandi R. and Fairchild I. J. (2013) Biogeochemical cycling of sulphur in karst and transfer into speleothem archives at Grotta di Ernesto, Italy. *Biogeochemistry* **114**, 255–267.

Wynn P. M., Fairchild I. J., Spötl C., Hartland A., Mattey D., Fayard B. and Cotte M. (2014) Synchrotron X-ray distinction of seasonal hydrological and temperature patterns in speleothem carbonate. *Environ. Chem.* **11**, 28–36.

Wynn P. M., Fairchild I. J., Borsato A., Spötl C., Hartland A., Baker A., Frisia S. and Baldini J. U. L. (2018) Sulphate partitioning into calcite: Experimental verification of pH control and application to seasonality in speleothems. *Geochim. Cosmochim. Acta* **226**, 69–83.

Zhou H. Y., Zhao J. X., Wang Q., Feng Y. X. and Tang J. (2011) Speleothem-derived Asian summer monsoon variations in Central China during 54–46 ka. *J. Quat. Sci.* **26**, 781–790.

Associate editor: Heather Stoll